



HAL
open science

Optimal dip based on dissipation of back thrusts and hinges in fold-and-thrusts belts

Bertrand Maillot, Y.M. Leroy

► **To cite this version:**

Bertrand Maillot, Y.M. Leroy. Optimal dip based on dissipation of back thrusts and hinges in fold-and-thrusts belts. *Journal of Geophysical Research*, 2003, 108, B6 (B6), pp.2320-2237. 10.1029/2002JB002199 . hal-00068533

HAL Id: hal-00068533

<https://hal.science/hal-00068533>

Submitted on 28 Jan 2021

HAL is a multi-disciplinary open access archive for the deposit and dissemination of scientific research documents, whether they are published or not. The documents may come from teaching and research institutions in France or abroad, or from public or private research centers.

L'archive ouverte pluridisciplinaire **HAL**, est destinée au dépôt et à la diffusion de documents scientifiques de niveau recherche, publiés ou non, émanant des établissements d'enseignement et de recherche français ou étrangers, des laboratoires publics ou privés.

Optimal dip based on dissipation of back thrusts and hinges in fold-and-thrust belts

Bertrand Maillot

Département des Sciences de la Terre, UMR 7072, CNRS, Université de Cergy-Pontoise, Cergy-Pontoise, France

Yves M. Leroy

Laboratoire de Mécanique des Solides, UMR 7649, CNRS, École Polytechnique, Palaiseau, France

Received 12 September 2002; revised 29 January 2003; accepted 28 February 2003; published 28 June 2003.

[1] Back thrusts and hinges are two types of transition between rigid sections of hanging walls observed in fold-and-thrust belts. Back thrusts are typical of frictional and homogeneous solids and hinges of creeping and layered materials. Our objective is to study the orientation of these transitions for the special case of a lower flat-ramp transition in a fault-bend fold with the following general two-step methodology. In the first step, the forces acting on the transition are determined using equilibrium of each rigid section. In the second step, the optimal dip of the transition is obtained by minimizing the total dissipation of the structure. The three sources of dissipation, of comparable magnitude, are at the transition, on the flat, and on the ramp. For frictional material flows, the back thrusts are velocity discontinuities with optimal dips always less than half the complementary ramp angle, leading to hanging wall thickening. The optimal dip agrees well with the results of physical analogue and numerical experiments. For creeping and layered materials, it is shown that a destabilizing deformation mechanism, selected to be flexural slip, is necessary for the strain to localize and the existence of hinges to be justified. Activation of flexural slip reduces dissipation at the transition and affects the optimal transition dip. The two-step methodology proposed here could be seen as a first attempt in producing mechanically balanced cross sections accounting for material rheology. This approach should complement the now classical kinematic models of folding. *INDEX TERMS*: 8005 Structural Geology: Folds and folding; 8020 Structural Geology: Mechanics; 8030 Structural Geology: Microstructures; 8102 Tectonophysics: Continental contractional orogenic belts; *KEYWORDS*: fold, thrust, dissipation, mechanics, tectonics, rheology

Citation: Maillot, B., and Y. M. Leroy, Optimal dip based on dissipation of back thrusts and hinges in fold-and-thrust belts, *J. Geophys. Res.*, 108(B6), 2320, doi:10.1029/2002JB002199, 2003.

1. Introduction

[2] Outer zones of mountain belts are often characterized by a horizontal shortening of the shallow sedimentary pile below which the basement remains undeformed. The decollement planes or flat thrusts are shallower toward the exterior of the belt because of a series of ramps that the upper plate must climb (see Figure 1 for terminology). The transition from a flat thrust to an inclined ramp is thus ubiquitous in those so-called thin-skinned fold-and-thrust belts. The first objective of this paper is to find the tectonic forces acting on these transitions using the special case of a single lower flat-ramp transition as an example. The second objective is to provide an evaluation of the orientation of the transition based on a minimization of the total dissipation of the structure.

[3] The transitions defined above, which are observed in the field, in physical analogue modeling and numerical

simulations can be classified into three categories, depending on the activated deformation mechanisms and on the friction on the ramp and on the flat. The first category is composed of smooth transitions with a diffuse curvature. Materials conducive to such transitions include viscous fluids having no destabilizing agents to trigger strain localization, as studied theoretically by *Berger and Johnson* [1980, 1982] and by *Wiltschko* [1981], with application to the Pine Mountain thrust block in the Appalachian mountains. Cohesive and frictional materials such as unconsolidated sand could also lead to smooth transitions if underlain by a viscous material, to dampen the effects of the sharp contact between the flat thrust and the ramp, and also to reduce the ramp friction. These two effects are clearly seen in analogue experiments [*Merle and Abidi*, 1995] and in the field as, for example, in the western Montana thrust belt [*Serra*, 1977]. In the presence of friction on the lower flat and the ramp, cohesive and frictional materials accommodate the passage on the ramp by a series of regularly spaced and dipping back thrusts which constitutes the second category of transitions. Field examples include thrust faults

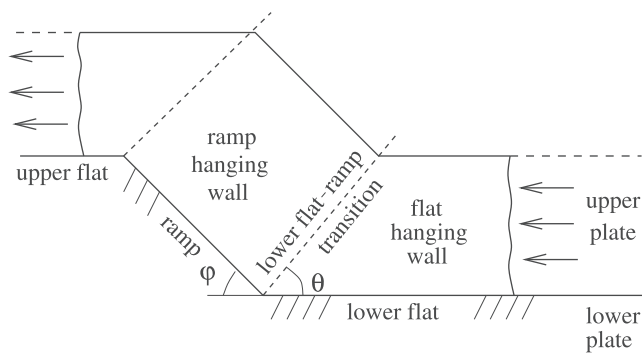


Figure 1. Terminology used to describe the geometry of a generic fault-bend fold. The lower flat-ramp transition is called back thrust in frictional materials and hinge in creeping materials.

in the Banff formation and in the Casper mountain, Alberta [Serra, 1977]. Such sharp transitions have also been studied with physical modeling in the laboratory [Morse, 1977; Chester *et al.*, 1991]. The back thrust dip depends on the frictional properties of the thrust planes, as observed in analogue [Merle and Abidi, 1995] and numerical [Erickson *et al.*, 2001] experiments. The third category of transitions is observed in kink folds and is composed of hinges of finite thickness which separate the various straight limbs. They are present in thin-skinned fold-and-thrust belts, as in the Rundle thrust of the Canadian Rocky Mountains, Alberta, the Snake River Range, Wyoming [it Boyer, 1986], in the Ougarta Range, Algeria [Collomb and Donzeau, 1974], and were already suggested by Rich [1934] in his study of the Cumberland thrust block of the Appalachian belt. The existence of these transition zones, in the form of hinges of finite thickness, is often related to the layered nature of sedimentary rocks constituting the upper plates of the thrust planes. Of particular interest here is the case of the so-called fixed hinges, relative to the lower plate, and through which the material of the upper plate is convected to follow the inclined ramp. Such fixed hinges have been inferred from field observations as in the Umbrian-Marches Apennines, Italy [Geiser, 1988], the South East Lost Hills, California [Medwedeff, 1989], and the Santa Barbara Channel, California [Shaw and Suppe, 1994]. The presence of these fixed hinges is also a common hypothesis of most kinematic models proposed to study ramp related folds such as the fault-bend fold and the fault-propagation fold models [Suppe, 1983; Suppe and Medwedeff, 1984, 1990].

[4] Kinematic models can reproduce field observations despite the absence of any assumptions on the material rheology (apart from volume conservation) and of any basic concepts of mechanics such as equilibrium and strain-displacement compatibility. This paper could be seen as a first attempt to palliate to this deficiency and to introduce mechanics in kinematic models. As a preliminary step, it is proposed to study the last two categories of transitions for which the deformation is localized in the form of back thrusts or hinges. The analysis of the equilibrium of every rigid block provides the forces acting on the transitions and at the origin of the various sources of dissipation. The minimization of the total dissipation is then proposed to find

the optimal orientation of the transition. These two points are considered for two rheologies corresponding to frictional and viscous materials.

[5] The accommodation by a sharp transition of the change in orientation of a sheet first horizontal and then having to climb an inclined ramp is not restricted to structural geology and has been studied extensively in engineering in the context of the orthogonal metal cutting process [Merchant, 1944, 1945]. Despite the differences in time and length scales, the analogy between the geological back thrusts or hinges and the transition created in metal cutting deserves some attention. The horizontal layer for metal cutting is fixed and corresponds to the thin layer of material removed from the machined piece by an advancing tool, which plays the role of the ramp. Merchant [1945] proposes to estimate the orientation of the transition zones by minimizing the work done by the advancing tool and which is dissipated by friction on the tool face (the ramp) and in the transition zone. The same approach will be followed here to estimate the orientation of the back thrusts for frictional materials deforming on geological times. The need to optimize the rate of cutting in high-speed machining has lead engineers to reconsider recently the work of Merchant. The sharp transition first seen as a discontinuity is then analyzed as a thin shear zone through which the strain rate and temperature sensitive material is convected. At sufficiently high tool velocities, the material thermal softening is activated and leads to strain localization and thus to a favorable reduction in the force applied to the tool [Molinari and Dudzinski, 1992; Bodin, 1996]. A similar analysis is considered here to study the internal structure of hinges. Flexural slip is proposed as the appropriate destabilizing factor to explain the strain localization.

[6] Flexural slip has been accounted for to reproduce kink fold geometry with anisotropic viscous rheologies [Lan and Hudleston, 1997; Johnson and Johnson, 2002a, 2002b]. There is however in these studies no explicit link to the microstructure since the rheologies of the beds and the interbed slip are not differentiated. Other accounts of flexural slip in folding analysis include the stratified viscoplastic structure of Erickson and Jamison [1995], proposed to explore the stress distribution during folding. The relevance of a destabilizing factor to trigger strain localization is not explored in their numerical experiments. It will be shown here that such a destabilizing factor is necessary to explain the existence of sharp transitions. An example of destabilizing factor is the nonassociated plasticity flow rule considered by Erickson *et al.* [2001], which is responsible for the strain localization in the form of back thrusts observed in their numerical simulations, as it could be inferred from the seminal work of Rudnicki and Rice [1975]. The destabilizing effect is obtained here by describing flexural slip through a two-phase continuum model of creeping flow. The first phase is the bulk and the second is the interfaces. The second phase is weaker in the sense that the viscosity of the whole is reduced once slip is activated. This weakening is the destabilizing factor which leads to strain localization.

[7] The contents of this paper are as follows. The prototype for the lower flat-ramp transition is presented in section 2 starting with the geometry and the equilibrium

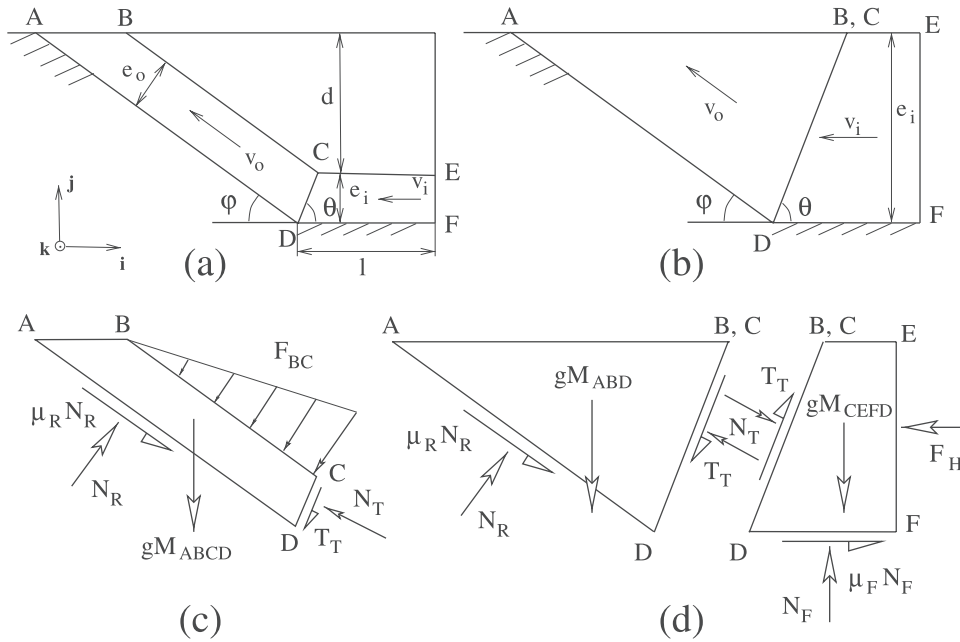


Figure 2. (a) Model problem of a layer (CEFD) which slides rigidly toward the transition zone (CD) where it sustains the simple shear deformation necessary to climb rigidly over the ramp (AD) before reaching the top surface at (AB) where the material is eroded away. (b) Same model problem for the case where the layer (CEFD) reaches the surface. (c) and (d) Free body diagrams of the hanging wall (ABCD) for the cases in Figures 2a and 2b, respectively, used to compute the external forces N_T and T_T acting on the transition zone (CD).

of the hanging wall above the ramp and the flat regions. The prototype geometry is essentially 2-D but could be generalized to 3-D to study lateral ramps, as it was already done by *Merchant* [1944] in the context of oblique metal cutting. The equilibrium of the rigid regions provides the forces acting on the transition zone. Section 2 continues with the introduction of the rheology for frictional materials as well as for the two-phase creeping solids which will permit localization in the hinges. Section 3 is concerned with the dissipation of the structure for frictional materials, the transition zone being a back thrust, i.e., a discontinuity in the velocity field. The dissipation is shown to have three sources of comparable magnitude which are the frictions over the ramp, the back thrust, and the flat. It is proposed that the transition dip minimizing the dissipation is the most favorable. This optimal orientation does not bisect the ramp complementary angle, a condition necessary to preserve the hanging wall thickness. This optimal orientation is also independent of the flat length. The relevance of this optimal orientation is justified by comparing the predictions with observations made with analogue [*Bonini et al.*, 2000; *Merle and Abidi*, 1995] and numerical [*Erickson et al.*, 2001] experiments. Sections 4 to 7 deal with the steady flow of the two-phase creeping material through the fixed hinge. The flow, up to the onset of flexural slip, has an analytical solution presented in section 4. The strain localization, necessary to explain the existence of hinges, is analyzed in section 5, the numerical algorithm being presented in Appendix A. Section 6 provides a discussion of potential tectonic markers based on a detailed analysis of the stress field in the hinge. Section 7 pertains to the analysis of the dissipation in the

hinge for the creeping two-phase material. The activation of flexural slip leads to a reduction of dissipation by a factor of up to four. This dissipation, as for the case of back thrusts, exhibits a minimum in terms of the transition dip which does not correspond to the bisection of the complementary angle. The generalization of the two-step procedure, determination of the forces acting on the transition and minimization of the dissipation, to obtain mechanically balanced cross sections, is discussed in section 8.

2. Prototype for a Lower Flat-Ramp Transition

[8] The objective of this section is to present the boundary value problem proposed to study the transition from a lower flat to an inclined ramp in ramp related folds. The geometry of the prototype and the hypotheses of the modeling are first presented. Further assumptions concerning the rheology of the frictional materials and of the creeping two-phase solids, characteristic of the two types of transitions studied, are then presented before a dimensional analysis is provided.

2.1. Prototype Geometry and Equilibrium of the Hanging Wall

[9] The prototype proposed to study the transition zones in a fault-bend fold is shown in Figure 2a. It consists of the layer (CEFD) of thickness e_i and length l buried at the depth d which is moving to the left to enter the transition zone defined by the line (DC) with a dip θ . The layer then moves up the ramp dipping with the angle φ . Note that the two angles φ and θ are independent and thus the classical

assumption of kinematic models [Suppe, 1983] that the hinge bisects the complementary angle of the ramp (i.e., $2\theta + \varphi = \pi$) is not adopted here. The layer on the ramp has for thickness e_o and reaches the surface at (AB). It is assumed that erosion is fast and erases immediately any structural relief so that the top surface remains flat for any velocity of the horizontal layer denoted v_i . The flow through the transition zone is thus stationary, and further assumed to be isochoric. The geometry of the proposed prototype is sufficiently general for analyzing the two types of transitions, back thrusts and hinges. In the case of back thrusts, we let the hanging wall reach the top surface (i.e., the burial depth $d = 0$), as shown in Figure 2b.

[10] There are two consequences to the hypotheses of stationary isochoric flow through the transition. First, entry and exit velocities, the latter denoted v_o , must have the same component perpendicular to the hinge, denoted V , such that

$$v_o \sin(\theta + \varphi) = v_i \sin \theta = V. \quad (1)$$

Second, the material flux through the transition zone is constant ($v_i e_i = v_o e_o$) providing the following relation:

$$e_o = e_i \frac{\sin(\theta + \varphi)}{\sin \theta}, \quad (2)$$

between the thickness of the layer before and after crossing the line (DC) (Figure 2a). The thickness variation predicted by equation (2) only occurs if the transition does not bisect the ramp complementary angle.

[11] The free-body diagram of section (ABCD) presented in Figure 2c summarizes the external forces in action for the geometry of Figure 2a. Section (AB) is free of forces and it is assumed that the resultant tangential force along (AD) is equal in magnitude to the resultant normal force N_R times the friction coefficient along the ramp μ_R . This friction coefficient is related to a friction angle α_R with the usual relation: $\tan \alpha_R = \mu_R$. The sediments above the line (BC) are assumed to be poorly consolidated, and thus to be in a hydrostatic stress state governed by the lithostatic pressure. The total force F_{BC} is thus normal to the section (BC) and its magnitude is $\rho g d^2 / (2 \sin \varphi)$ in terms of the volumic mass ρ and the gravity acceleration g . The last external force is the weight of the section which is denoted gM_{ABCD} in Figure 2c. The two equilibrium equations for the forces acting on the section (ABCD) are in terms of the unknowns N_R , the tangential force T_T and the normal force N_T over (DC). These two equations are combined to eliminate the unknown N_R providing the following relation between the two components T_T and N_T :

$$\begin{aligned} N_T \sin(\theta + \varphi + \alpha_R) + T_T \cos(\theta + \varphi + \alpha_R) \\ = \rho g \frac{2d + e_i}{2} e_i \frac{\sin(\theta + \varphi)}{\sin \theta} \frac{\sin(\alpha_R + \varphi)}{\sin \varphi} + \rho g \frac{1}{2} d^2 \frac{\sin \alpha_R}{\sin \varphi}, \end{aligned} \quad (3)$$

while the first (i.e., equilibrium in direction \mathbf{i} , Figure 2) is presented to determine N_R

$$N_R \frac{\sin(\alpha_R + \varphi)}{\cos \alpha_R} - T_T \cos \theta - N_T \sin \theta = \rho g \frac{1}{2} d^2. \quad (4)$$

Note that in equation (3), the mass M_{ABCD} has been replaced by the expression for the surface (ABCD) times the volumetric mass ρ , selected to be the same as above the line (BC). Note also that the moment of the forces which have been described above has also to be zero. This third equilibrium equation could be used to estimate the distribution of external forces on the ramp but that information is not required in what follows.

[12] The second equilibrium analysis concerns the geometry of Figure 2b for the special case of a thick hanging wall reaching the top surface. The linear relation between N_R , N_T and T_T in equation (4) still applies (setting $d = 0$) but, for the determination of the dissipation on the flat, one needs to find the equilibrium of section (CEFD), for which a free-body diagram is shown in Figure 2d. Equilibrium of that section requires

$$\begin{aligned} F_H - N_F \tan \alpha_F - N_T \sin \theta - T_T \cos \theta &= 0, \\ N_F - N_T \cos \theta + T_T \sin \theta - \rho g e_i \left(l - \frac{1}{2} e_i \cot \theta \right) &= 0, \end{aligned} \quad (5)$$

in terms of F_H and N_F which are the horizontal force responsible for the movement of the whole structure to the left and the normal reaction of the flat thrust, respectively.

2.2. First Type of Transition: Back Thrust in Frictional Materials

[13] Back thrusts are defined as velocity discontinuities along which the material has attained its critical strength limit. This limit is expressed by the Mohr-Coulomb relation between the resolved shear stress and the normal stress. Since this critical stress condition is enforced at every point along the transition (CD), the following relation between tangential force and normal force is thus supposed to hold

$$T_T \cos \alpha_B - N_T \sin \alpha_B = 0, \quad (6)$$

in which α_B is the friction angle of the material (the friction coefficient is $\mu_B = \tan \alpha_B$). Relation (6) is the only assumption on the material response required to study the orientations of back thrusts in section 3.

2.3. Second Type of Transition: Hinge in Creeping Two-Phase Materials

[14] The line (CD) presented in Figure 2a is now presented as the region (CC'DD') on a smaller length scale in Figure 3, revealing the inner structure of the hinge. It is assumed that the material sustains a deformation, which is an overall simple shear, only through the hinge. The thickness of the sheared region h is assumed to be small compared to the bed thickness e_i which, in turn, is small compared to the burial depth d . The flow through the hinge can then be assumed independent of the x_1 coordinate, defining the lateral position along the hinge, and thus function of x_2 only, which is the position through the hinge. The coordinate system is introduced in Figure 3 with the three basis vectors (\mathbf{e}_1 , \mathbf{e}_2 , \mathbf{e}_3), the first being along the hinge. Vectors, as well as tensors, are identified by bold characters. The independence of the flow on the position along the hinge means also that the details of the flow close to the two ends (CC') and (DD') are not analyzed.

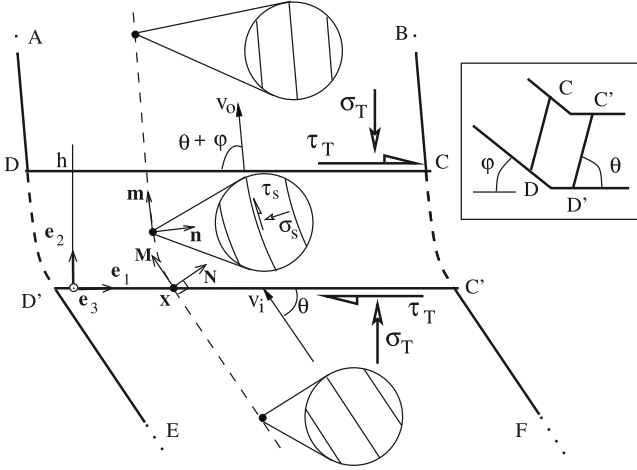


Figure 3. Transition zone presented as a single line (CD) in Figure 2a shown as a hinge (CC'DD') through which the material is convected. The resulting simple shear mode of deformation in the hinge is assumed to be described only in terms of the x_2 coordinate and thus to be independent of the x_1 coordinate. The material at the microscale (circular insets) is composed of a bulk phase and of interfaces which are horizontal before the hinge and parallel to the ramp after having sustained the overall simple shear.

[15] The rock material has the microstructure shown at the three points marked by a solid dot in Figure 3. It is constituted of a bulk material as well as of interfaces initially parallel to the bedding and convected by the transformation to become parallel to the ramp after their passage through the hinge. The ratio of the average distance between two interfaces to the size of the representative volume element is $1 - \phi$ so that the dimensionless number ϕ , referred to as the flexural slip density, is close to one for finely spaced interfaces.

[16] The velocity field \mathbf{U} in the hinge is stationary and, since the flow is isochoric, can be written as

$$\mathbf{U}(x_2) = U_1(x_2)\mathbf{e}_1 + V\mathbf{e}_2, \quad (7)$$

in terms of the single unknown function $U_1(x_2)$ of the position x_2 of a particle at \mathbf{x} . This particle was initially at $\mathbf{X} = X_1\mathbf{e}_1 + X_2\mathbf{e}_2$ ($X_2 = 0$), the entry of the hinge, at a time set arbitrarily to zero, i.e., $\mathbf{X} = \mathbf{x}$ ($t = 0$). The velocity field provides the equations for the trajectories of the particles through the hinge which are

$$x_1(\mathbf{X}, t) = X_1 + \int_0^t U_1(x_2(\mathbf{X}, t')) dt', \quad x_2(\mathbf{X}, t) = Vt. \quad (8)$$

These trajectories are tangent to the streamlines because of the stationary flow assumption. This fact is now used to orient the microstructure defined by the tangent \mathbf{m} and the normal vectors \mathbf{n} of the slip planes in a particle at \mathbf{x} . This particle at the entrance of the hinge was at \mathbf{X} and its microstructure was then oriented with the normal $\mathbf{N} = \sin\theta\mathbf{e}_1 + \cos\theta\mathbf{e}_2$ and tangent $\mathbf{M} = -\cos\theta\mathbf{e}_1 + \sin\theta\mathbf{e}_2$. Because the flow is stationary, the material vector \mathbf{M} is convected by the transformation to the vector \mathbf{m} at \mathbf{x} , parallel to the velocity

vector. Consequently, the vector \mathbf{m} and the normal to the slip surface \mathbf{n} are given by

$$\begin{aligned} \mathbf{m}(x_2) &= \frac{U_1(x_2)\mathbf{e}_1 + V\mathbf{e}_2}{(V^2 + U_1(x_2)^2)^{1/2}}, \\ \mathbf{n}(x_2) &= \frac{V\mathbf{e}_1 - U_1(x_2)\mathbf{e}_2}{(V^2 + U_1(x_2)^2)^{1/2}}. \end{aligned} \quad (9)$$

The Eulerian gradient of the velocity field is computed from equation (7) and its symmetric part is the rate of deformation tensor

$$\mathbf{D} = D_{ij}\mathbf{e}_i \otimes \mathbf{e}_j = \dot{\gamma} \frac{1}{2} (\mathbf{e}_1 \otimes \mathbf{e}_2 + \mathbf{e}_2 \otimes \mathbf{e}_1), \quad \dot{\gamma}(x_2) = \frac{dU_1(x_2)}{dx_2}, \quad (10)$$

in terms of the function $\dot{\gamma}(x_2)$ which is introduced as a shorthand notation for the derivative with respect to x_2 of the velocity component $U_1(x_2)$. The tensorial product \otimes introduced in equation (10) acts between two vectors \mathbf{a} and \mathbf{b} resulting in a second-order tensor defined by $(\mathbf{a} \otimes \mathbf{b}) \cdot \mathbf{c} = \mathbf{a} (\mathbf{b} \cdot \mathbf{c})$ for any vector \mathbf{c} (see, for example, Chadwick [1999], for further comments). The rate of deformation in equation (10) is a simple shear mode of deformation. This simple shear is accommodated by a material composed of two phases. The first phase is the bulk which is incompressible and deforms according to a power law rheology so that the relation between the Cauchy stress and the rate of deformation tensor \mathbf{D}_B sustained by that phase is

$$\boldsymbol{\sigma} = -p\mathbf{I} + \frac{2\tau_{0B}}{\dot{\gamma}_{0B}} \left(\frac{\dot{\gamma}_B}{\dot{\gamma}_{0B}} \right)^{m_B-1} \mathbf{D}_B, \quad \dot{\gamma}_B = (2\mathbf{D}_B : \mathbf{D}_B)^{1/2}, \quad (11)$$

in which p , \mathbf{I} , τ_{0B} , $\dot{\gamma}_{0B}$, m_B and $\dot{\gamma}_B$ are the pressure, the second-order identity tensor, a reference stress, a reference strain rate, the strain rate sensitivity exponent and the equivalent strain rate based on \mathbf{D}_B , respectively. The notation “:” introduced in equation (11) and employed between two second-order tensors \mathbf{A} and \mathbf{B} should be interpreted as the trace of the second-order tensor resulting from the product $\mathbf{A} \cdot \mathbf{B}$, i.e., $\mathbf{A} : \mathbf{B} = \text{tr}(\mathbf{A} \cdot \mathbf{B}) = A_{ik}B_{ki}$. Note that the incompressibility constraint requires that the trace of the tensor \mathbf{D}_B (i.e., its first invariant) be zero whereas the plane strain assumption is satisfied by imposing that D_{B33} be zero. These two remarks will have some important consequences on the structure of the stress state which will be discussed at the end of this section. The second phase present at any point \mathbf{x} is the interfaces which can accommodate slip along the direction \mathbf{m} , defined in equation (9), so that the rate of deformation tensor due to slip is

$$\mathbf{D}_S = \dot{\gamma}_S \frac{1}{2} (\mathbf{m} \otimes \mathbf{n} + \mathbf{n} \otimes \mathbf{m}), \quad (12)$$

in terms of the equivalent strain rate for slip $\dot{\gamma}_S(x_2)$. The tensorial structure of equation (12) is similar to the one found in equation (10). It corresponds to a simple shear in the basis (\mathbf{m}, \mathbf{n}) constituted by the slip plane and its normal.

The equivalent strain rate $\dot{\gamma}_S$ is function of the stress and the following rheology for slip is adopted

$$\dot{\gamma}_S = \phi \dot{\gamma}_{0S} \left(\frac{|\tau_S| + \mu_S \sigma_S}{\tau_{0S}} \right)^{n_S} \text{Sign}(\tau_S), |\tau_S| + \mu_S \sigma_S > 0. \quad (13)$$

The strain rate $\dot{\gamma}_S$ is zero otherwise: slip is activated only if a Mohr-Coulomb criterion (without cohesion) is met on the slip (i.e., stratigraphic) planes. Upon activation, the behavior of the slip planes is that of a non-Newtonian fluid. The power law introduced in equation (13) is based on $\dot{\gamma}_{0S}$, τ_{0S} , n_S and Sign which are a reference strain rate for slip, a reference stress, the stress exponent and the sign function, respectively. Note that the strain rate for slip is assumed to be proportional to the density of the second phase ϕ . The resolved shear and normal stress τ_S and σ_S introduced in equation (13) are defined by

$$\sigma_S = \mathbf{n} \otimes \mathbf{n} : \boldsymbol{\sigma}, \quad \tau_S = \frac{1}{2} (\mathbf{m} \otimes \mathbf{n} + \mathbf{n} \otimes \mathbf{m}) : \boldsymbol{\sigma}, \quad (14)$$

in terms of the Cauchy stress (see, again, *Chadwick* [1999] for a full definition).

[17] It is assumed that the overall simple shear mode of deformation given in equation (10) results from the sum of the rates of deformation sustained by the two phases

$$\mathbf{D} = \mathbf{D}_B + \mathbf{D}_S. \quad (15)$$

It should be noted that if slip occurs then the strain rate due to the interfaces \mathbf{D}_S , defined in equation (12), is not proportional to the overall simple shear introduced in equation (10). Consequently, the bulk phase strain rate \mathbf{D}_B does not have the structure of a simple shear mode to satisfy the summation in equation (15).

[18] The complexity of the two-phase material rheology requires solution of a boundary value problem for mechanical equilibrium to determine the flexural slip distribution through the hinge. The stress state and the boundary conditions for that problem are now discussed. To be consistent with the 1-D assumption of the transformation, the external forces found in equation (3) are distributed uniformly over the length (CD) leading to the introduction of two external force densities

$$\sigma_T = N_T \frac{\sin \theta}{e_i}, \quad \tau_T = T_T \frac{\sin \theta}{e_i}, \quad (16)$$

which are the boundary conditions for the stress state in the hinge, as illustrated in Figure 3. The Cauchy stress in the hinge satisfies equilibrium $\text{div}(\boldsymbol{\sigma}) = 0$, disregarding gravity forces over the hinge vertical extension compared to the tectonic load due to burial and friction on the ramp. The solution of these equilibrium equations for a stress state, which is only a function of the x_2 coordinate, implies that σ_{12} and σ_{22} be equal to τ_T and to $-\sigma_T$ at every point through the hinge. Further information on the stress can be obtained by recognizing that according to equation (11) and since the bulk phase is incompressible, the deviatoric stress state is proportional to the rate of deformation tensor \mathbf{D}_B . The material flow satisfies the plane strain condition requiring furthermore that there is no deviatoric stress in the third

Table 1. Parameter Definitions, Units, Values Considered in the Simulations, and Reference Values

Parameter	Unit	Value	Reference ^a
h hinge thickness	m	10	h_R
e_i nappe thickness	m	50	h_R
d burial depth	m	1000, 800	h_R
ρg volumic weight	Pa/m	2.2×10^4	σ_R/h_R
θ hinge dip	—	75°	—
φ ramp dip	—	30°	—
μ_R ramp friction	—	0.2	—
v_i shortening velocity	mm/yr	[0.35, 10]	h_R/t_R
<i>Bulk Phase</i>			
$\dot{\gamma}_{0B}$ reference strain rate	1/s	2.2×10^{-14}	$1/t_R$
τ_{0B} reference stress	Pa	1.1×10^5	σ_R
m_B strain rate exponent	—	1	—
<i>Slip Phase</i>			
$\dot{\gamma}_{0S}$ reference strain rate	1/s	2.2×10^{-14}	$1/t_R$
τ_{0S} reference stress	Pa	2.2×10^3	σ_R
μ_S friction	—	0.1	—
n_S stress exponent	—	1	—
ϕ density of surfaces	—	0.7	—

^aReference values are $h_R = 10$ m, $\sigma_R = 0.22$ MPa, $t_R = 0.45 \times 10^{14}$ s = 1.44 Ma.

direction. These two conditions lead to the following structure of the stress state in the hinge

$$\boldsymbol{\sigma} = (\sigma_T - 2p(x_2))\mathbf{e}_1 \otimes \mathbf{e}_1 - \sigma_T \mathbf{e}_2 \otimes \mathbf{e}_2 - p(x_2)\mathbf{e}_3 \otimes \mathbf{e}_3 + \tau_T(\mathbf{e}_1 \otimes \mathbf{e}_2 + \mathbf{e}_2 \otimes \mathbf{e}_1), \quad (17)$$

in terms of the unknown function $p(x_2)$ introduced in equation (11) and the scalar τ_T which is related to σ_T through equations (16) and (3). It is shown in Appendix A how these unknowns are determined numerically in the presence of slip along the interfaces. The analytical solution without flexural slip, discussed in section 4, serves to predict the onset of flexural slip.

[19] The final part of this section is devoted to the dimensional analysis and to a discussion of the rheological parameters selected for the two-phase viscous material. Table 1 gives parameter values used in the two simulations presented in section 5 and summarizes this dimensional analysis. Dimensionless values are obtained by dividing the dimensional values by their reference value. The reference value for length is arbitrarily set to a hinge thickness $h_R = 10$ m. The reference value for stresses is then $\sigma_R = \rho g h_R = 0.22$ MPa, with the reference volumic weight of the sediments ρg set to 22 kPa/m. Although still difficult to determine precisely [e.g., *Renard et al.*, 2000], bulk rock viscosities are expected to range from 10^{17} to 10^{21} Pa s. Choosing a reference viscosity $\eta_R = 10^{19}$ Pa s leads to a reference time $t_R = \eta_R/\sigma_R = 4.545 \times 10^{13}$ s = 1.44 Ma, a reference velocity $V_R = h_R/t_R = 2.2 \times 10^{-13}$ m/s = 6.94×10^{-3} mm/yr, and a reference strain rate $\dot{\gamma}_R = 1/t_R = 2.2 \times 10^{-14}$ s⁻¹.

[20] A discussion of the rheological parameters is now in order to explain the possibility for the deformation to localize at shallow depths and thus to justify the existence of hinges. The studied structure is buried at a depth less than 5 km so pressure and temperature are of the order of 100 MPa and 100°C. Having in mind a rock such as calcite, we could expect fluid-assisted deformation mechanisms to be activated [Gratier, 1993]. The strain rate exponent m_B appearing in equation (11) must thus be of the order of 1 (Figure 4). The reference viscosity η_R then defines the ratio $\tau_{0B}/\dot{\gamma}_{0B}$. At such

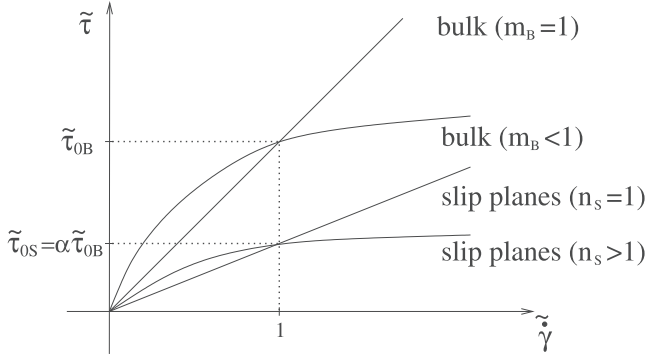


Figure 4. Definition of the rheology adopted for the bulk and the slip planes which are the two phases constituting the creeping. The normalized stress and strain rate represent the equivalent shear stress and strain rate for the former and the resolved shear stress and slip rate for the latter. For both linear and nonlinear rheology, the slip planes are thought of as the weak phase so that its activation results in a weakening of the material responsible for strain localization (i.e., $\alpha < 1$). The normalization is based on the data found in Table 1.

shallow depths, temperature sensitivity cannot explain an unstable creeping flow. Furthermore, deformation by twinning, which could be destabilizing, is limited to small strains and must therefore be activated prior to the entry of the hinge. It is disregarded in this study. Flexural slip thus appears to be the only potential candidate for explaining localization and is introduced in our modeling for this reason. A linear viscosity function is also adopted for the creep of the second phase (the interfaces). Such a linear viscosity function is certainly stable in shear and it is the combination of the two phases which is destabilizing for reasons now discussed. Note first, from Figure 4, that the viscosity of the weak interfaces is selected to be only a fraction α ($\alpha = \tau_{0S}/\tau_{0B} = 0.02$ for the data of Table 1) of the bulk phase viscosity. This remark is true for the linear and the power law creep relations. The consequence is that the flow is stiffer in the absence of flexural slip. The triggering of the weak second phase is thus a destabilizing mechanism, leading to strain localization, as it will be seen in section 5.

3. Dissipation With a Back Thrust in Frictional Materials

[21] The objective of this section is to determine the optimum orientation of the back thrust to minimize the total dissipation in the structure. There are three sources of dissipation, by friction on the ramp, on the back thrust, and on the flat thrust. These three contributions are first analyzed before conducting the minimization of the total dissipation. Our calculations are conducted for the particular case of d set to zero shown in Figure 2b.

[22] The first source of dissipation is over the ramp and corresponds to the power of the tangential force $\mu_R N_R$ times the velocity v_o of the ramp hanging wall. Using relation (1) to relate entry and exit velocities, the dissipation is then written as

$$D_R = \tan \alpha_R \frac{\sin \theta}{\sin(\theta + \varphi)} N_R v_i. \quad (18)$$

The second source of dissipation is along the back thrust and is computed as the product of the tangential force N_T times the jump in tangential velocity $v_i \cos \theta - v_o \cos(\theta + \varphi)$. The dissipation D_B is then expressed as

$$D_B = \tan \alpha_B \frac{\sin \varphi}{\sin(\theta + \varphi)} N_T v_i, \quad (19)$$

once relation (1) and the Mohr-Coulomb relation in equation (6) have been used. The third source of dissipation is over the flat thrust and is defined as the product of the horizontal reaction force by the horizontal velocity

$$D_F = \tan \alpha_F N_F v_i. \quad (20)$$

[23] To progress further, one needs to determine the forces N_R , N_T and N_F involved in equations (18), (19), and (20). These are easily found by proper combinations of the global equilibrium equations (3), (4), and (5), with the Mohr-Coulomb criterion equation (6). N_T is found by combining equation (3) with equation (6). N_R is found in terms of N_T by use of equations (4) and (6), while N_F results from the combination of equation (5) with equation (6).

[24] The sum of the three expressions (18), (19), and (20), is the total dissipation, which can be written as

$$D = D_R + D_F + D_B = F v_i,$$

with

$$\begin{aligned} F &= k(\theta, \varphi, \alpha_R, \alpha_B, \alpha_F, l/e_i) \rho g \frac{e_i^2}{2}, k(\theta, \varphi, \alpha_R, \alpha_B, \alpha_F, l/e_i) \\ &= \frac{\sin(\theta + \alpha_B)}{\sin(\theta + \varphi + \alpha_R + \alpha_B)} \frac{\sin \alpha_R}{\sin \varphi} + \frac{\sin(\varphi + \alpha_R) \sin \alpha_B}{\sin \theta \sin(\theta + \varphi + \alpha_R + \alpha_B)} \\ &\quad + \tan \alpha_F \left[2 \frac{l}{e_i} - \cot \theta + \frac{\sin(\theta + \varphi) \sin(\varphi + \alpha_R) \cos(\theta + \alpha_B)}{\sin \theta \sin \varphi \sin(\theta + \varphi + \alpha_R + \alpha_B)} \right], \end{aligned} \quad (21)$$

in which F and k are termed the tectonic force and the tectonic factor, respectively. The tectonic force is conjugate to the entry velocity v_i in the sense of dissipation. The tectonic factor k is the tectonic force normalized by the characteristic weight of the structure which is $\rho g e_i^2/2$. This factor is a function of the two angles θ , φ , of the aspect ratio l/e_i which define the geometry, and of the frictional properties of the ramp, the back thrust, and the flat thrust (α_R , α_B , α_F). The three terms appearing in equation (21) correspond to the contributions of the ramp, the back thrust, and the flat, respectively.

[25] The minimum of k with respect to θ is assumed to provide the optimum orientation of the back thrust. This minimum θ_m satisfies the implicit relation

$$\begin{aligned} \sin^2 \theta_m &= \sin(2\theta_m + \varphi + \alpha_R + \alpha_B) \frac{\sin \alpha_B}{\sin \alpha_R} \sin \varphi \\ &\quad - \frac{\sin \varphi \tan \alpha_F}{\sin \alpha_R \sin(\varphi + \alpha_R)} \sin^2(\theta_m + \varphi + \alpha_R + \alpha_B) - \frac{\tan \alpha_F}{\sin \alpha_R} \\ &\quad \cdot [\cos(2\theta_m + \varphi + \alpha_B) \sin \theta_m \cdot \sin(\theta_m + \varphi + \alpha_R + \alpha_B) \\ &\quad - \sin(\theta_m + \varphi) \cdot \cos(\theta_m + \alpha_B) \sin(2\theta_m + \varphi + \alpha_R + \alpha_B)], \end{aligned} \quad (22)$$

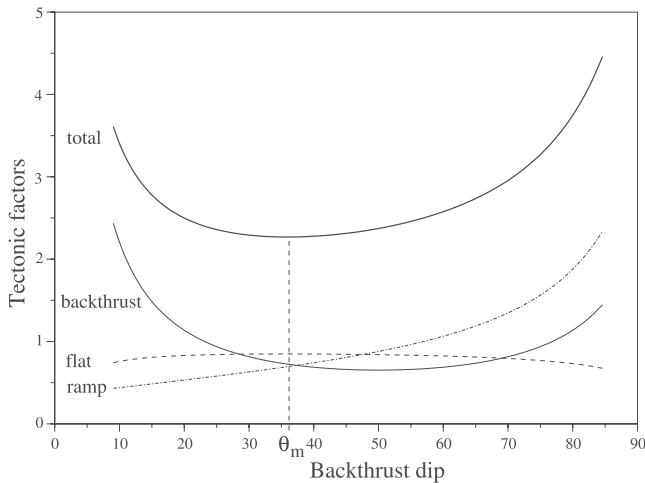


Figure 5. Tectonic factors (equation (21)) for the back thrust, the ramp, and the flat thrust (solid, dash-dotted, and dashed curves, respectively) as functions of the back thrust dip θ in degrees. The thick solid curve is the sum of the others. Parameters are those of data set 2 of Table 2 ($\alpha_R = 20^\circ$, $\alpha_B = 30^\circ$, $\varphi = 30^\circ$), except for $\alpha_F = 5^\circ$ in order to show the dependence of the dissipation on the flat with respect to the back thrust dip. The flat thrust length was set to $l = 5e_i$.

obtained by setting to zero the derivative of k in equation (21) with respect to θ . Note that the flat length l and the hanging wall thickness e_i do not appear in this equation. The optimal back thrust dip with respect to dissipation is thus function only of the frictional properties (α_B , α_R , α_F) and of the ramp dip (φ).

[26] The three sources of dissipation are now analyzed with the help of Figure 5. The thick solid line represents the variation of the tectonic factor k with respect to the back thrust dip θ for $\alpha_R = 20^\circ$, $\alpha_F = 5^\circ$, $\alpha_B = 30^\circ$, $\varphi = 30^\circ$, and $l/e_i = 5$. The three other curves (dash-dotted, solid, and dashed) correspond respectively to the three sources, i.e., to the contributions of the ramp, the back thrust, and the flat thrust. They show that all three sources of dissipation are of comparable magnitudes and thus that none can be disregarded in analyzing the total dissipation of the structure. Furthermore, dissipation over the ramp (dash-dotted curve) is an increasing function of the back thrust dip and thus the ramp friction tends to make the back thrust horizontal. Friction in the back thrust tends to preclude high and low dips since it exhibits a minimum at intermediate dips (thin solid curve). Friction over the flat thrust, to the contrary, tends to promote either low or high back thrust dips, although it is less sensitive than the two other sources of dissipation (dashed curve). The global optimal back thrust dip ($\theta_m = 36^\circ$) is the result of these three competing effects.

[27] The principle of minimum dissipation is not fundamental to mechanics and its application needs to be justified. It is for that reason that our predictions for back thrust orientation are now compared to some published observations on analogue and numerical experiments. Table 2 presents six data sets chosen as to reproduce the observations of *Erickson et al.* [2001] (data sets 1 and 2), *Bonini et al.* [2000] (data sets 3 and 4), and *Merle and Abidi* [1995] (data sets 5 and 6). The optimal back thrust dip θ_m predicted

by equation (22) is provided, as well as the observed values θ^* . The observations of *Erickson et al.* [2001, Figures 4 and 11a] are numerical experiments of back thrusts as shear bands in an elastoplastic material obtained with the frictional parameters listed in the data sets 1 and 2. They show that the ramp friction has a strong influence on the back thrust dip: changing the ramp friction angle from 0° to 20° reduces the back thrust dip from 60° to 39° . The same variation leads to a change in our prediction of θ_m from 60° to 36° . The observations of *Erickson et al.* [2001] are thus well predicted by our methodology.

[28] *Bonini et al.* [2000] conducted a series of sand box experiments with $\alpha_B = 30^\circ$ (data sets 3 and 4 of Table 2). Contrary to our assumption, there is no erosion of the relief building up above the ramp, so we can only compare back thrust dips at small reliefs. This corresponds to the experiments with a ramp dip $\varphi = 15^\circ$ in the work by *Bonini et al.* [2000]. The main difference with our model problem of Figure 2b is that the sand layer in the analogue experiment is fixed relative to the flat thrust. It is the ramp that is moving rigidly toward the sand layer. The comparison with our model is not straightforward, explaining the selection of two extreme cases with $\alpha_F = 0^\circ$ and $\alpha_F = 30^\circ$. Furthermore, the friction coefficient of the sand against the rigid plexiglass ramp is not given. Choosing $\alpha_R = 20^\circ$ yields a very good fit between our prediction of θ_m (32.5°) and the observed back thrust dip $\theta^* = 33^\circ$, in both cases $\alpha_F = 0^\circ$ and $\alpha_F = 30^\circ$. Choosing $\alpha_R = 25^\circ$ yields $\theta_m = 29^\circ$ for the two values of α_F . These results confirm the important influence of the ramp friction on θ_m , and the relative insensitivity of θ_m to the flat friction.

[29] Data sets 5 and 6 of Table 2 are an attempt to reproduce the sand box experiments of *Merle and Abidi* [1995, experiments RE9 and RE18], where a sand layer resting on plexiglass (RE9) or on silicone (RE18) is pushed toward a plexiglass rigid ramp dipping at $\varphi = 30^\circ$, and is eroded (RE9) or not (RE18). In RE9, back thrusts dip between 37° and 45° and in RE18 their dip is approximately 30° . Two effects can be invoked to explain these variations of dip: the friction on the flat (strong for plexiglass, weak for silicone) and the erosion. The preceding examples have shown that the friction on the flat alone cannot explain these differences. Now, to account in a simple manner for the build up of relief above the ramp, a higher friction coefficient is assigned to the ramp if there is no erosion compared to the case with erosion (our data set 5 for experiment RE9 and data set 6 for RE18). This variation in friction coefficient is sufficient to vary the predicted back

Table 2. Comparison of Predicted and Observed Back Thrust Dips for Six Sets of Parameters^a

	1	2	3	4	5	6
α_R	0	20	20	20	15	25
α_F	0	0	0	30	15	0
α_B	30	30	30	30	30	30
φ	30	30	15	15	30	30
θ_m	60	36	32.5	32.5	40	33
θ^*	60(1)	39(1)	33(2)	33(2)	37 to 45(3)	30(3)

^aThe optimal back thrust dip θ_m is the solution of equation (22) and the observed back thrust dips θ^* are from 1, *Erickson et al.* [2001]; 2, *Bonini et al.* [2000]; and 3, *Merle and Abidi* [1995]. These data appear as solid diamonds, an open diamond, and dots, respectively, on Figures 6a and 6c.

thrust dip from 33° to 40° , two values which are close to the two observations done in the laboratory. In summary, the respective roles of the ramp friction and dip have been well captured: increasing the ramp friction decreases the back thrust dip. The ramp dip has the same, but less pronounced influence. Finally, all examples presented above, and the unscaled physical experiments of *Morse* [1977] and *Chester et al.* [1991] exhibit, in agreement with our predictions, back thrust dips that do not bisect the ramp complementary angle. They always lead to a thickening of the hanging wall (ranging from 15% to 80% for the data of Table 2).

[30] The general behavior of the optimal back thrust dip (equation (22)) is summarized in Figure 6, where θ_m is plotted as a function of the ramp dip (Figure 6a), the back thrust friction (Figure 6b), and the ramp friction (Figure 6c). Figure 6 could also be used by the reader to search for the optimum dip based on other data sets than the ones proposed here and shown as solid diamonds [*Erickson et al.*, 2001], an open diamond [*Bonini et al.*, 2000], and dots [*Merle and Abidi*, 1995]. The influence on θ_m of the friction on the flat is too weak to deserve further discussion: the friction angle could be changed from 0° to 30° without a noticeable change on the curves. Three curves are presented in each graph, the solid curves corresponding to $\alpha_R = 20^\circ$, $\alpha_B = 30^\circ$, $\varphi = 30^\circ$, the dashed curves, to $\alpha_R = 0.5^\circ$, $\alpha_B = 20^\circ$, $\varphi = 30^\circ$, and the dotted curves, to $\alpha_R = 20^\circ$, $\alpha_B = 30^\circ$, $\varphi = 15^\circ$, except for the parameter selected to draw the plot. The ramp dip and the back thrust friction angle α_B have essentially the same influence on θ_m : there is a maximum value, which is of the order of 70° , reached for the lowest value of the ramp friction angle, Figures 6a and 6b. This influence of α_R is confirmed in Figure 6c, where θ_m is seen to be a decreasing function of that argument. Note that all curves of Figure 6 indicate back thrust dips that are always much below the dip necessary to conserve the thickness of the upper plate (i.e., $\theta = (\pi - \varphi)/2$).

[31] To conclude, minimizing the total dissipation leads to a prediction of the back thrust dip which is consistent with the analogue and numerical experiments discussed above. The present comparisons can certainly be improved since the friction parameters are rarely provided in the publications on analogue experiments. Furthermore, these experiments are always designed to study complex geometries compared to the ones considered here. A dedicated series of analogue experiments would thus be beneficial to complete the validation of the present methodology.

4. Onset of Flexural Slip in the Hinge

[32] Sections 4–7 are devoted to transitions defined as hinges of finite thickness with the two-phase viscous material rheology described in section 2 (equations (7) to (17)). This section is concerned with the onset of flexural slip.

[33] In the absence of slip along the stratigraphic planes, $\mathbf{D}_S = 0$, and the material sustains a homogeneous simple shear equation (10) corresponding to the velocity field

$$\mathbf{U}(x_2) = v_i \left(-\cos\theta + \frac{\sin\varphi}{\sin(\theta + \varphi)} \frac{x_2}{h} \right) \mathbf{e}_1 + V \mathbf{e}_2. \quad (23)$$

The resulting stress state is

$$\boldsymbol{\sigma} = \tau_T (\mathbf{e}_1 \otimes \mathbf{e}_2 + \mathbf{e}_2 \otimes \mathbf{e}_1) - \sigma_T \mathbf{I}, \quad (24)$$

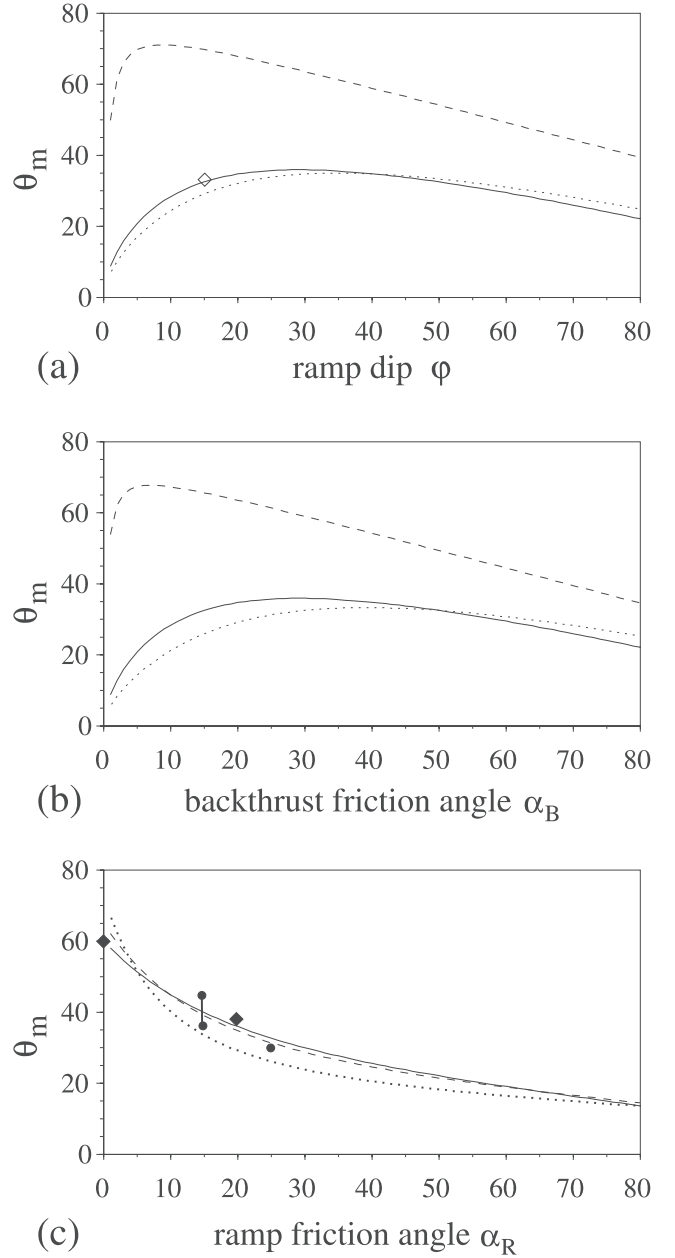


Figure 6. Predicted optimal back thrust dip θ_m as a function of the ramp dip, the back thrust friction angle and the ramp friction. The friction angle α_B , which has no noticeable effect, is set to zero. The three curves are obtained for $\alpha_R = 20^\circ$, $\alpha_B = 30^\circ$, $\varphi = 30^\circ$ (solid curves); $\alpha_R = 0.5^\circ$, $\alpha_B = 20^\circ$, $\varphi = 30^\circ$ (dashed curves); $\alpha_R = 20^\circ$, $\alpha_B = 30^\circ$, $\varphi = 15^\circ$ (dotted curves), except for the parameter selected to vary. Diamonds and dots are published data (see Table 2).

obtained by identifying the general expression of the stress state equation (16) with the bulk phase behavior (equation (11)). The pressure is thus equal to $p(x_2) = \sigma_T (\nabla x_2)$, and the shear stress is

$$\tau_T = \tau_{0B} \left(\frac{v_i \sin\varphi}{h \dot{\gamma}_{0B} \sin(\theta + \varphi)} \right)^{m_B}, \quad (25)$$

the two quantities being uniform over the domain.

[34] Flexural slip is triggered first in the hinge where the Mohr-Coulomb criterion (13) is met on the stratigraphic plane. This point, noted x_2^s , and the shortening velocity v_i^s required to trigger flexural slip are now determined, using the graphical constructions of Figure 7. The principal stresses according to equation (24) are $(\sigma_T + \tau_T, \sigma_T - \tau_T)$ and their directions are $(\mathbf{e}_2 - \mathbf{e}_1, \mathbf{e}_2 + \mathbf{e}_1, \mathbf{e}_3)$ with respect to the hinge framework $(\mathbf{e}_1, \mathbf{e}_2, \mathbf{e}_3)$ (Figure 3). Figure 7b shows that the stratigraphic planes enter the hinge making an angle $\beta_i = \theta - \pi/4$ with respect to the maximum principal stress, and exit with an angle $\beta_o = \theta + \varphi - \pi/4$. In the hinge, this angle is

$$\beta(x_2) = \frac{3\pi}{4} - \arctan\left(\frac{V}{U_1(x_2)}\right), \quad (26)$$

where $U_1(x_2)$ is given by equation (23). The most favorable orientation for slip is, from Figure 7a, $\beta(x_2^s) = \beta_s = \pi/4 - \alpha_S/2$, where $\alpha_S = \arctan \mu_S$ is the friction angle of the stratigraphic planes. Thus solving this last equation for x_2^s provides the position

$$x_2^s = h \left(\cos \theta - \sin \theta \tan \frac{\alpha_S}{2} \right) \frac{\sin(\theta + \varphi)}{\sin \varphi}. \quad (27)$$

The critical velocity v_i^s is now determined by considering the stresses required for slip. From the construction of Figure 7a, there is slip if $\tau_T = \sigma_T \sin \alpha_S$. Combining this condition for slip with the global equilibrium condition (3), and the expression for τ_T (equation (25)) yields

$$\begin{aligned} v_i^s = h & \frac{\dot{\gamma}_{0B}}{\tau_{0B}^{1/m_B}} \frac{\sin(\theta + \varphi)}{\sin \varphi} \left[\frac{\rho g}{2e_i} \frac{\sin \alpha_S}{\sin \varphi} ((2d + e_i) \cdot e_i \sin(\theta + \varphi)) \right. \\ & \cdot \sin(\varphi + \alpha_R) + d^2 \sin \theta \sin \alpha_R (\sin(\theta + \varphi + \alpha_R)) \\ & \left. + \sin \alpha_S \cos(\theta + \varphi + \alpha_R) \right]^{-1} \frac{1}{m_B}. \end{aligned} \quad (28)$$

The position x_2^s and critical velocity v_i^s depend on the hinge thickness h which is here arbitrarily set. However, the ratios x_2^s/h and v_i^s/h are independent of h . In other words, the relative location of the initiation of slip and the time spent by an element of rock in the hinge at the onset of slip are both independent of the hinge thickness. Finally, Figure 7a shows that flexural slip may be triggered only if $\beta_i \leq \beta_s \leq \beta_o$. This is not very restrictive and will be true in most cases. The predictions (27) and (28) will be used in section 5 to validate the numerical solution.

5. Strain Localization Due to Flexural Slip in the Hinge

[35] In this section we analyze the strain and stress distributions in the hinge beyond the onset of flexural slip for a fixed set of parameters. The role of these parameters is then discussed. The solution in the presence of slip is not analytical and requires a numerical approach. The finite element method used to compute the velocity and stress profiles through the hinge is presented in Appendix A.

5.1. Example of Strain Localization

[36] An example of strain localization by flexural slip is now proposed for the set of parameters given in Table 1.

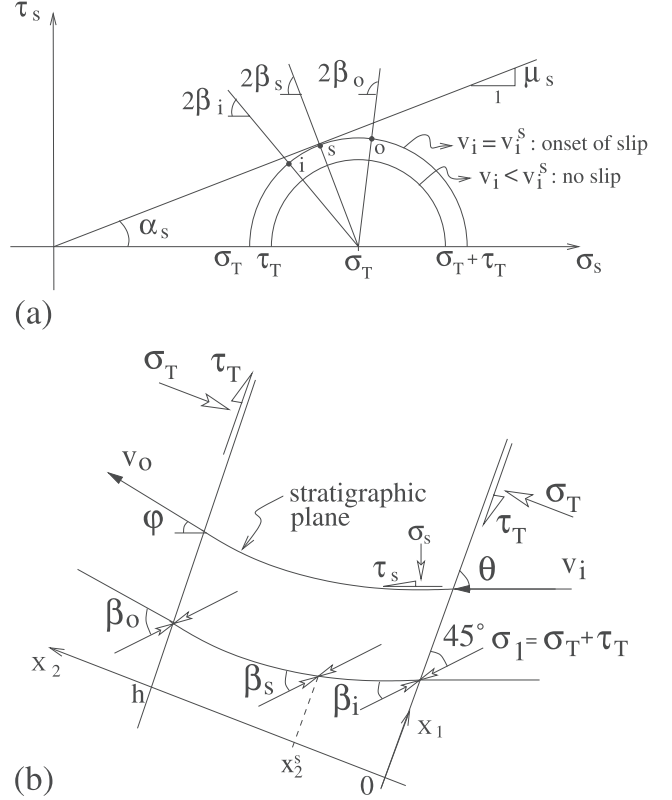


Figure 7. Onset of flexural slip determined graphically by the Mohr-Coulomb criterion $\tau_s = \mu_s \sigma_s$ in terms of the resolved shear and normal stresses on the stratigraphic planes. (a) Plot showing that these planes which could accommodate slip enter and exit the hinge at points i and o of the Mohr circle, respectively. The point s is where slip first occurs if the shortening velocity v_i is equal to v_i^s . (b) An equivalent representation in the physical space showing the position x_2^s where flexural slip is first triggered. Analytic formulae for x_2^s and v_i^s are given by equations (27) and (28).

The burial depth is $d = 1000$ m, and the ramp dips at $\varphi = 30^\circ$, with a friction $\mu_R = 0.2$. In agreement with the one-dimensional assumption ($d \gg e_i \gg h$), we consider the passage through the hinge of thickness $h = 10$ m, and dip $\theta = 75^\circ$, of a material of thickness $e_i = 50$ m. The bulk phase has a linear ($m_B = 1$) viscosity $\tau_{0B}/\dot{\gamma}_{0B} = 0.5 \times 10^{19}$ Pa s, and density of slip surfaces $\phi = 0.7$. Slip has also a linear ($m_S = 1$) viscosity $\tau_{0S}/\dot{\gamma}_{0S} = 10^{17}$ Pa s (Figure 4), and a friction $\mu_S = 0.1$. The shortening velocity v_i ranges from 0.35 to 10 mm/yr.

[37] Figure 8 shows the velocity profiles $U_1(x_2)$ through the hinge for various shortening velocities v_i . The first curve of Figure 8, for $v_i = 1.58$ mm/yr, follows the analytic solution (23) given for the case without flexural slip, thus confirming the accuracy of the numerical solution. Furthermore, the finite element solution predicts the onset of flexural slip for $v_i^s = 1.6$ mm/yr, at the position $x_2^s = 0.41h$, in agreement with the analytic solutions (27) and (28). Other velocity profiles are nonlinear, showing increasing gradients with the shortening velocity in the zone of flexural slip, and decreasing gradients away from this zone,

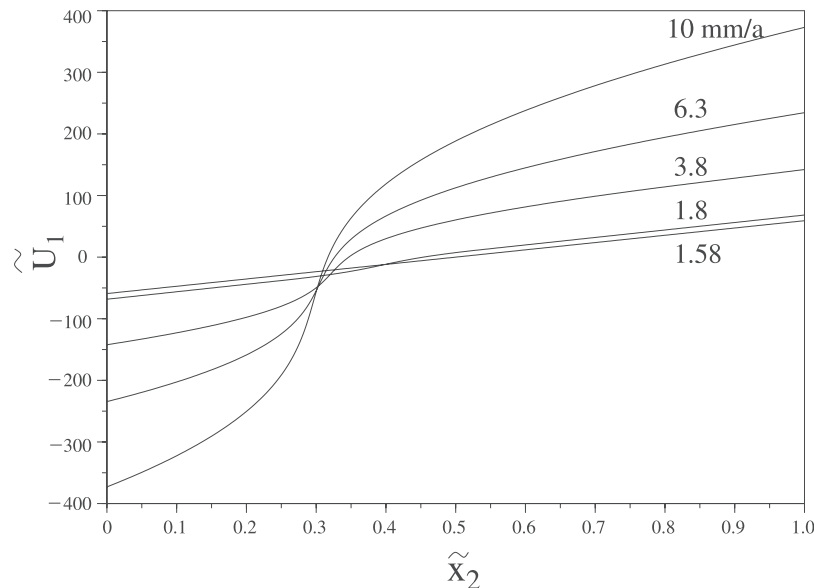


Figure 8. Normalized lateral velocity profiles $\tilde{U}_1(\tilde{x}_2)$ through the hinge for increasing shortening velocities v_i from 1.58 to 10 mm/yr. All other parameter values are constant and given in Table 1. The linear profile for $v_i = 1.58$ mm/yr coincides with the analytic solution (24) in the absence of flexural slip. All other (nonlinear) profiles show the effect of flexural slip, the onset of which coincides with the analytical predictions of equations (27) and (28), at the position $\tilde{x}_2 = 0.41$, for a velocity $v_i = 1.6$ mm/yr.

as can be better observed on the profiles of total strain rate $\dot{\gamma}$, and slip rate $\dot{\gamma}_S$ of Figures 9a and 9b. The equivalent strain rate $\dot{\gamma}$ is larger by one order of magnitude at the point of maximum flexural slip compared to the entrance and exit of the hinge, for a shortening velocity $v_i = 10$ mm/yr. This is a clear expression of the localization of the deformation concomitant with the triggering of the flexural slip, which acts as a destabilizing mechanism. It should be noted that localization occurs in the absence of any strain rate softening in either phase, both being linearly viscous. It is the activation of the weak phase, composed of interfaces, which reduces the strength of the material.

[38] The first component of the rate of deformation tensor in the bulk phase (representing the extensional strain rate along the hinge) and the pressure p are presented in Figures 9c and 9d, respectively, as functions of the position x_2 . The shear stress $\tilde{\tau}_T$ is uniform and takes the values 97, 81, and 61 (or 21, 18, and 13 MPa, respectively), for the three curves of Figure 9d (corresponding to $v_i = 10$, 6.3, and 1.8 mm/yr, respectively). The pressure at the entrance and exit of the hinge ($\tilde{x}_2 = 0$ and 1) for low velocities v_i corresponds to the normal force density acting on the hinge $\sigma_T = \tilde{p}(0)\sigma_R = 600 \times 0.22 = 132$ MPa. It should be noted that this pressure is six times the lithostatic pressure, because of the necessity to equilibrate the friction exerted by the ramp on its hanging wall. The pressure decreases from the hinge entrance to reach a minimum, then increases to take a maximum value before decreasing again toward the exit. This variation is coupled to a positive extensional rate in $D_{B_{11}}$ in the first part of the hinge and a negative, compressional, rate closer to the hinge exit. These variations within the hinge of the pressure and the bulk rate of deformation are necessary to accommodate the incompatibility of the slip on the interfaces with respect to the overall simple shear mode of deformation, as it was already suggested in section 2 (equation (15)). This

thickening/thinning sequence across the hinge of a kink fold is a well known observation, particularly visible in chevron folds, and should not be mistaken with the change in hanging wall thickness (equation (2)) implied by the conservation of the mass flux.

5.2. Parametric Study

[39] A full parametric study of the solutions with flexural slip is beyond the scope of the present paper. We nevertheless examine briefly the respective roles of the various parameters of the model and draw some intuitive conclusions. In particular, interest is focused on the influence of the burial depth.

[40] The Mohr representation of the stresses in the hinge (Figure 7a) indicates clearly that the amount of flexural slip, i.e., the size of the slipping zone and the magnitude of the slip rate, increases with the shear force density τ_T and decreases with the normal force density σ_T since the principal stresses are functions of these force densities applied at the boundaries. Understanding the role of the parameters therefore amounts to understanding their effects on the force densities at the hinge boundaries. Decreasing the hinge thickness h , or increasing the shortening velocity v_i , or the ramp dip φ , will increase the overall simple shear strain rate, and thus the shear stress τ_T , promoting localization. Localization will further be promoted by stiffening the bulk phase (increasing τ_{0B} , decreasing m_B or $\dot{\gamma}_{0B}$, in equation (11)), or softening the bed parallel slip rheology (decreasing τ_{0S} , n_S or increasing $\dot{\gamma}_{0S}$ in equation (13)). The burial depth d , the upper plate thickness e_i , and the ramp friction μ_R will control the normal stress on the hinge, and thus lessen localization when they are increased.

[41] The burial depth d deserves further attention. Figure 10 shows two solutions for the same shortening velocity $v_i = 1.8$ mm/yr for a depth $d = 1000$ m (solid

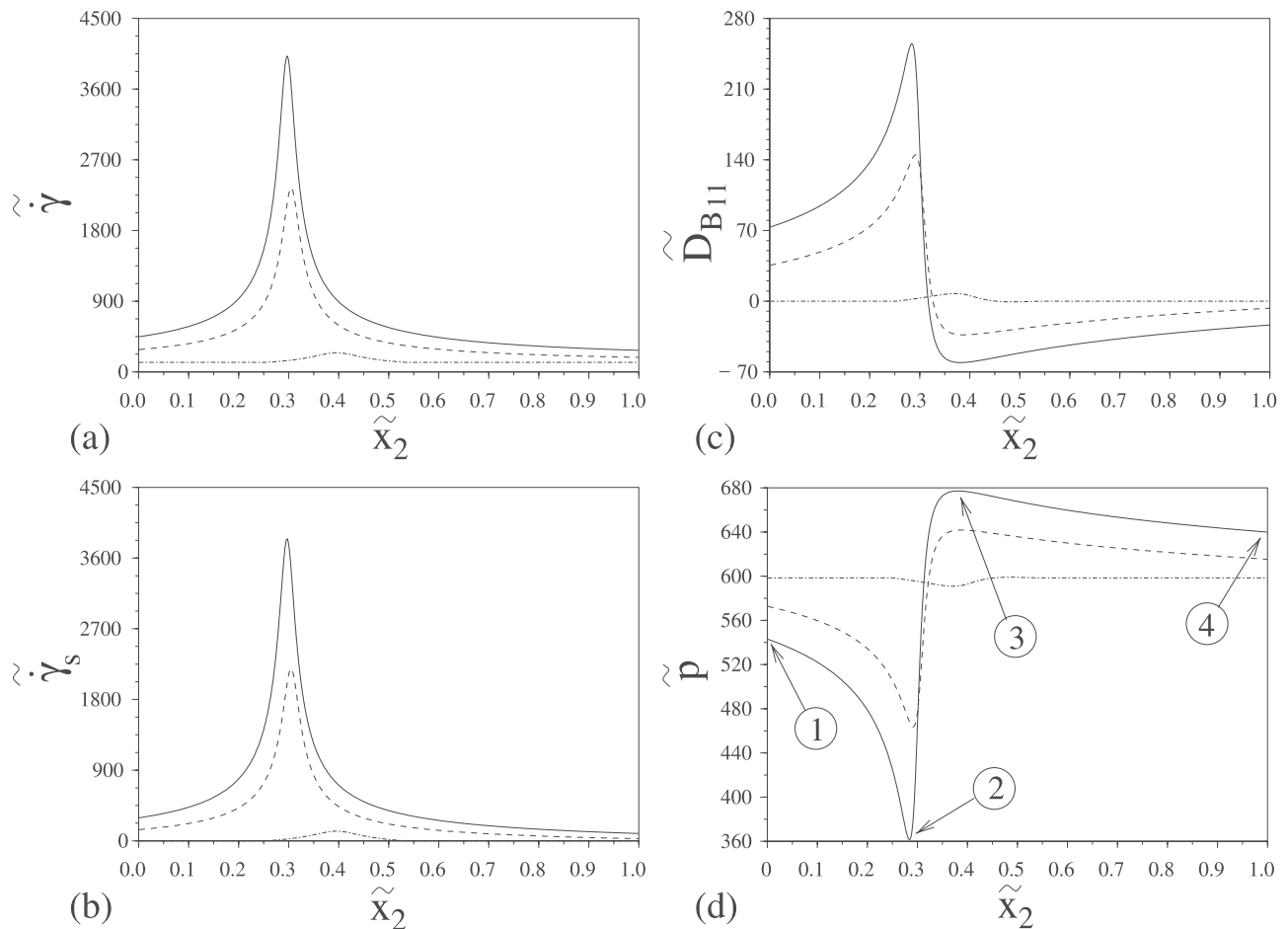


Figure 9. Profiles through the hinge of (a) the normalized simple shear strain rate $\tilde{\gamma}$, (b) bed parallel slip rate $\tilde{\gamma}_s$, (c) bed thickening rate \tilde{D}_{B11} , and (d) pressure \tilde{p} . Solid, dashed, and dash-dotted curves are for a shortening velocity $v_i = 10, 6.3,$ and 1.8 mm/yr, respectively. All other parameter values are constant, and given in Table 1. The normalized normal stress acting on the boundaries of the hinge is $\tilde{\sigma}_T = 600$ for all curves, while the normalized boundary shear stress is $\tilde{\tau}_T = 97, 81,$ and 61 for the solid, dashed and dash-dotted curves, respectively. The full stress states of points numbered 1 to 4 along the solid curve in Figure 9d are represented as Mohr circles in Figure 12.

curves) and $d = 800$ m (dashed curves), all other parameters being identical. The strain rate at the shallower depth is increased by a factor of two compared to its value at the greater depth. Similarly, the slip strain rate is increased by a factor of three. Moreover, it can be seen that the region where slip occurs is doubled in size as the depth is changed from 1000 to 800 m. This trend is confirmed by the distribution of the first component of the rate of deformation tensor in the bulk (Figure 10c). The ease to slip at shallow depth is understood from Figure 10d, where the pressure in the hinge is seen to increase by a factor of 50% as the depth increases by 25%. These results suggest, as it was foreseen above, that localization based on flexural slip, which is pressure sensitive, is more developed at shallower depths. This depth dependence of the slip zone could be used to motivate the need for a 2-D solution to the transition, then seen as a fan. This fan has a triangular shape with the tip at the foot of the ramp and opening toward the surface. Its width at any depth is likely to be well approximated in our 1-D analysis by the extent of the zone where slip takes place. This suggestion to introduce a

fan at the back transition has recently been proposed, on completely different grounds, in a new kinematic model [Cristallini and Allmendinger, 2002; Buil, 2002].

6. Implications of the Stress State in the Hinge

[42] We now present some geological consequences of the stress distributions with flexural slip by calculating the dips of potential microfractures and stylolitic joints.

[43] The numerical solution for the pressure field (Figure 9d) with the stress structure equation (17) provides the orientation of the maximum principal stress with respect to the hinge axis (\mathbf{e}_1 in Figure 3) which is plotted in Figure 11 and used to construct the Mohr circles in Figure 12. Circles 1 to 4 represent the stress state at the four points located in Figure 9d: on hinge entry, at the minimum and maximum pressure, and on hinge exit, for the solid curve only ($v_i = 10$ mm/yr). The most favorable position for the development of conjugate sets of microfractures, or for stylolitic joints, will always be at point 2 where the pressure is minimum and the differential stress reaches a maximum. At this point,

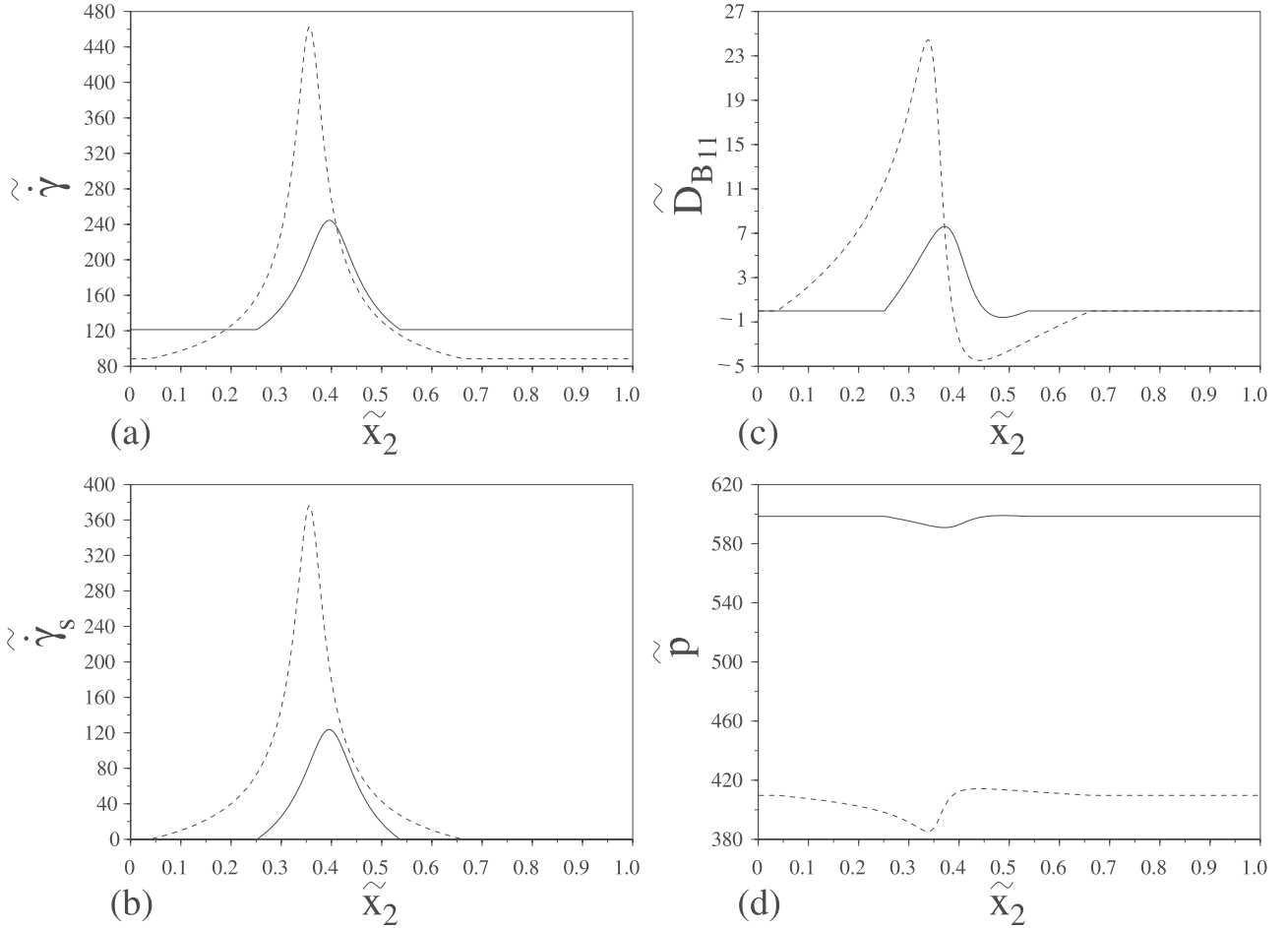


Figure 10. Illustration of the effect of the burial depth d . Same as Figure 9, for a shortening velocity $v_i = 1.8$ mm/yr. Solid curves are identical to the dash-dotted curves of Figure 9 for a burial depth $d = 1000$ m. The dashed curves correspond to a burial depth $d = 800$ m.

the dips of potential microfractures are, according to Figure 12,

$$d_f = \frac{\pi}{4} - \frac{\alpha_I}{2} \pm (\theta - \beta_m), \quad (29)$$

while those of potential stylolitic joints, assumed perpendicular to the maximum principal stress, are

$$d_s = \frac{\pi}{2} - \theta + \beta_m, \quad (30)$$

where α_I denotes the internal friction angle of the bulk phase, and β_m is the orientation of the maximum principal stress at point 2 (approximately -79° on Figure 11). In the present example (values in Table 1), and for $v_i = 10$ mm/yr and $\alpha_I = 30^\circ$, one obtains microfracture dips at 26° forward, and 34° backward, and stylolith dips at 84° forward. Note that a stylolitic joint growing during the convection through the hinge would exhibit a sigmoid shape due to the rotation of the maximum principal stress with respect to the bedding. Note also that to obtain dips outside of the hinge, i.e., in the hanging wall, one must also account for the convection of the microfractures from their position of formation to the exit of the hinge. This rotation can be

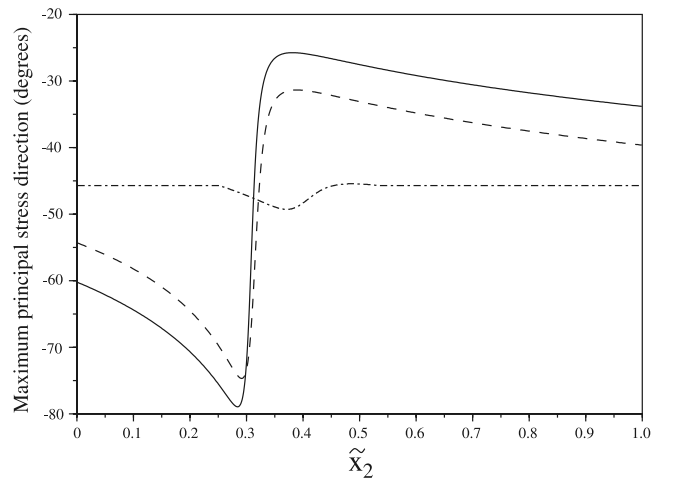


Figure 11. Angle between the maximum principal stress and the hinge axis (axis \mathbf{e}_1 in Figure 3) as a function of the normalized position in the hinge \tilde{x}_2 , counted positively in the anticlockwise sense. The entry velocity $v_i = 10$ mm/yr (solid curve), 6.3 mm/yr (dashed curve), and 1.8 mm/yr (dash-dotted curve). All other parameter values are constant and given in Table 1.

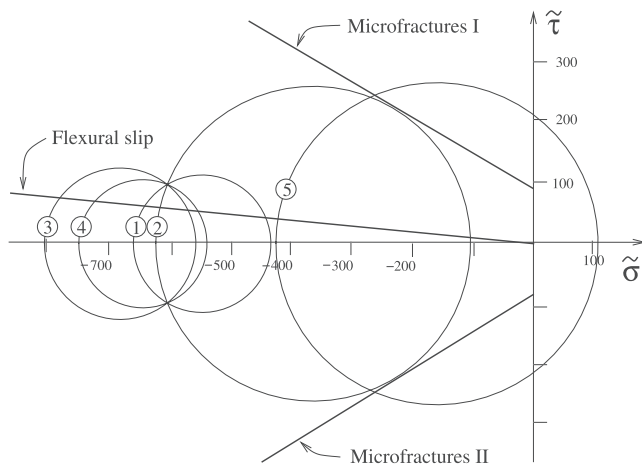


Figure 12. Mohr circles 1 to 4 illustrating the stress state in the hinge at the four positions indicated in Figure 10d for a shortening velocity $v_i = 10$ mm/yr. Axes are drawn with dimensionless values. The flexural slip envelop is everywhere overcome, thus indicating that bed-parallel slip occurs throughout the hinge. Point 2, where the pressure is minimum and the differential stress is maximum, is the location where one can expect conjugate sets of microfractures to form. The two points common to all four circles correspond to the stresses σ_T and τ_T acting on the boundaries of the hinge. Circle 5 is same as circle 2, but for a burial depth $d = 800$ m instead of 1000 m.

deduced by integrating the orientation of the principal stress equation (26) from the point 2 (with minimum pressure and maximum differential stress) to the exit of the hinge using the velocity distributions of Figure 8.

[44] Finally, the Mohr circle labeled 5 in Figure 12 is the same as circle 2, but for a burial depth $d = 800$ m instead of 1000 m. It shows the possibility of developing absolute extensional stresses within the hinge, even though the pressure outside the hinge ($\bar{p}(0)$ $\sigma_R = 410 \cdot 0.22$ MPa = 90 MPa, see Figure 10d) is 5 times greater than the lithostatic pressure at this depth, again, because of the ramp friction.

7. Dissipation in the Hinge

[45] The objective of this last section on the hinge with two-phase viscous materials is to study the dissipation in the transition. The model problem in Figure 2a serves the purpose of concentrating on the hinge and simplifying assumptions have been adopted for the rheology of the overburden. The dissipation in the hinge, because of its length, is then only a fraction of the dissipations on the ramp and the flat. A more realistic model would require to account, for example, for the dissipation along a series of kinks connecting the base of the ramp to the surface. The methodology would then be similar to the one described above for frictional materials: the sum of all sources of dissipation would be accounted for. It is proposed here for sake of conciseness, and in view of the simple structure proposed, to study only the dissipation in the hinge as a preliminary step. It is defined as the product of the change of lateral velocity before and after the hinge by the tangen-

tial force T_T . Using the kinematic relation (1) and the force density defined in equation (16), the dissipation reads

$$D_H = v_i e_i \tau_T \frac{\sin \varphi}{\sin \theta \sin(\theta + \varphi)}. \quad (31)$$

Following the decomposition proposed for the back thrust case (equation (21)), equation (31) is written as

$$D_H = F v_i, \quad \text{with } F = k \rho g \frac{e_i^2}{2}, \quad (32)$$

$$k = \frac{2}{\rho g e_i} \frac{\sin \varphi}{\sin \theta \sin(\theta + \varphi)} \tau_T,$$

where F and k are again termed the tectonic force and the tectonic factor, respectively, even though only the hinge is taken into account for computing the dissipation. In the absence of flexural slip, τ_T is given by equation (25), and thus

$$k = \frac{2 \tau_{0B} v_i}{\rho g e_i h \dot{\gamma}_{0B}} \frac{\sin^2 \varphi}{\sin \theta \sin^2(\theta + \varphi)}, \quad (33)$$

$$D_H = \frac{\tau_{0B} e_i}{h \dot{\gamma}_{0B}} v_i^2 \frac{\sin^2(\varphi)}{\sin \theta \sin^2(\theta + \varphi)}. \quad (34)$$

These analytic solutions are plotted as dotted curves on Figure 13 for a hinge dip $\theta = 70^\circ$ (Figures 13a and 13b) and a shortening velocity $v_i = 3$ mm/yr (Figures 13c and 13d). The tectonic factor is a linear function of the entry velocity v_i and dissipation is a quadratic function of the same argument. If flexural slip occurs, equations (33) and (34) do not apply and the stress τ_T is found by numerical means, as explained in Appendix A. The solutions for the tectonic factor and the dissipation are presented in Figures 13a and 13b as solid, dashed, and dash-dotted curves for a hinge dip of 60° , 70° , and 80° , respectively. The variation in hinge dip has little influence on the tectonic factor prior to the onset of slip (at $v_i = 1.6$ mm/yr, or $\tilde{v}_i = 230$). Beyond the onset, the tectonic factor is approximately linear again with the velocity, with a lower slope. It should be noted, even if it is not proven here, that the lower slope is sensitive to the density of slip surfaces ϕ and the contrast in viscosity between the bulk and the slip phases, two key parameters to enhance localization. In this example the dissipation is reduced by a factor of 4 for a velocity $v_i = 10$ mm/yr ($\tilde{v}_i = 1441$) between the cases with and without slip.

[46] Figures 13c and 13d show the tectonic factor for a range of velocities v_i as a function of the hinge dip. As in the back thrust case, both the tectonic factor and the dissipation in the hinge exhibit a minimum with respect to the hinge dip θ . For a realistic range of shortening velocities (3 to 9 mm/yr), the optimum hinge dip is between 63° and 73° , and therefore never equal to the dip of 75° assumed in all kinematic models. We would thus predict here a thickening of the ramp hanging wall between 12% and 2%, respectively. However, it should be kept in mind that this discussion is based on the hinge only. If the effect of the ramp is the same as in the back thrust case (Figure 5), then it

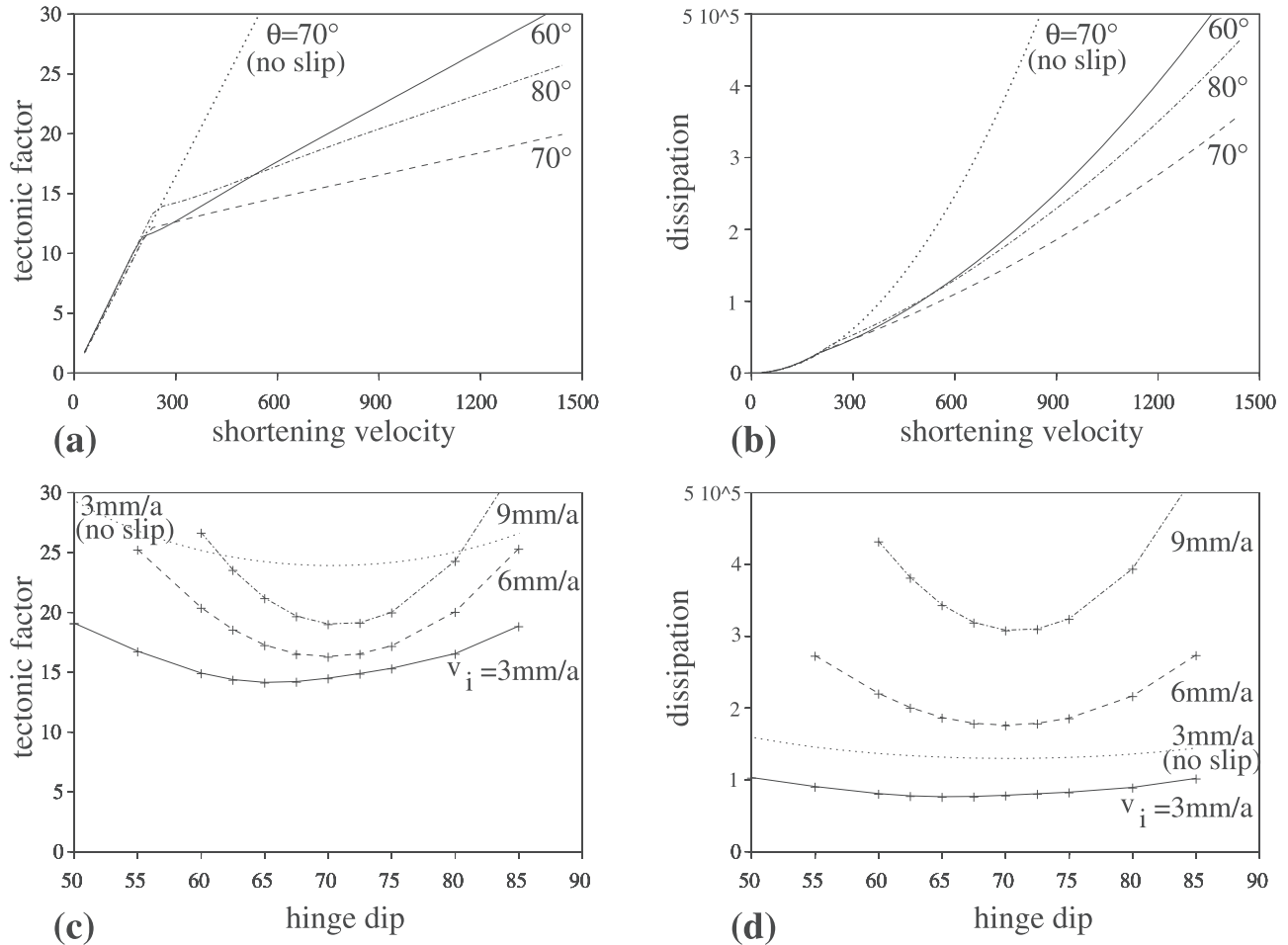


Figure 13. Analysis of the dissipation in the hinge. (a) and (b) Tectonic factor and dissipation (equation (32)) as functions of the dimensionless shortening velocity \tilde{v}_i . The solid, dashed, and dash-dotted curves are for $\theta = 60^\circ$, 70° , and 80° , respectively. (c) and (d) Tectonic factor and dissipation versus the hinge dip θ for $v_i = 3$, 6 , and 9 mm/yr (solid, dashed, dash-dotted curves, respectively). The dotted curves are the analytic solutions (33) and (34) in the absence of flexural slip, for a hinge dip $\theta = 70^\circ$ in Figures 13a and 13b and for a shortening velocity $v_i = 3$ mm/yr in Figures 13c and 13d.

would reduce considerably the optimal hinge dip found above, and further enhance the thickening.

8. Conclusion

[47] A general methodology has been proposed to study the transitions in the form of back thrusts and hinges within fault-related folds, using the special case of the lower flat-ramp transition as an example. The methodology consists of solving for the overall equilibrium of every rigid section to constrain the forces acting on the transitions. This information is then used to determine the various sources of dissipation. The dissipation at the transition depends on the rheology adopted for the convected material. Two cases have been considered: a frictional material leading to velocity discontinuities (back thrusts), once a Mohr-Coulomb criterion is satisfied, and a two-phase viscous material necessary to explain the strain localization in the hinges. The three sources of dissipation which are of similar magnitude are across the transition and by friction over the ramp and the flat. It is proposed that the dip of the transition rendering the total

dissipation minimum is the most likely to occur. This proposition is substantiated by comparing the predictions with the results of numerical and laboratory experiments.

[48] For the case of back thrusts, it is shown that the optimal dip is function of the ramp dip, and of the friction coefficients on the flat, the ramp and the back thrust. The optimal dip is independent of the flat thrust length even though the total dissipation is function of that length. Principle of minimum dissipation is not fundamental to mechanics even though it is known to provide upper bounds to failure load, which would be here the tectonic force responsible for thrusting. To justify the application of minimum dissipation principle, the optimal dip predicted has been compared and found to be in good agreement with the dip observed in sand-box [Bonini *et al.*, 2000; Merle and Abidi, 1995] and numerical [Erickson *et al.*, 2001] experiments. This comparison confirms that the optimal dip increases with decreasing ramp friction and ramp dip but is rather insensitive to the flat friction. The optimal dip is always less than the value required to conserve the thickness of the hanging wall.

[49] It is shown that fixed hinges, fundamental to kink folds, can be explained by the presence of a destabilizing factor in the rheology; the example of bedding parallel slip being proposed here. For that purpose, a two-phase rheological model has been constructed where the first phase is the bulk and creeps according to a linear or a power law viscosity function. The bed interfaces constitutes the second phase which has also a linear or a power law slip function, activated if a Mohr-Coulomb criterion is satisfied. Both phases sustain the same stress and the sum of their rate of deformation tensors define the strain rate of the whole. The second phase is weaker than the first in the sense that its activation leads to a reduction of the overall viscosity. It is the activation of slip which leads to an increase by an order of magnitude in the strain rate within the simple shear flow through the hinge. This slip is along stratigraphic planes and is thus not compatible with the overall simple shear. The bulk phase has to develop, after entry in the hinge, a positive extensional strain rate along the hinge and then a negative strain rate prior to the exit from the hinge to accommodate slip. This evolution of the creeping flow during its convection through the hinge is coupled to the pressure field within the hinge as follows: the pressure drops after entrance and sustains a minimum prior to a sharp increase toward a maximum and before decreasing again before exit from the hinge. This pressure gradient should result in the transport of fluids toward the region in positive extension rate which deserve further attention. It is also shown that the width of the zone where slip occurs within the hinge is sensitive to the depth because of the pressure-sensitive activation criterion adopted. The width is larger at shallower depth for the same velocity of the thrusting sheet suggesting a transition in the shape of a fan. Also, the activation of slip reduces the dissipation within the hinge. This dissipation has also a minimum with respect to the transition orientation, as for the case of back thrusts. That optimal dip would not bisect the lower flat-ramp angle, leading to a change in the hanging wall thickness which is disregarded in kinematic models.

[50] The general methodology outlined above for a single transition could be extended to structures with multiple transitions. It is conjectured that there exists a minimum in total dissipation which defines the optimal orientation of the various transitions. This line of research differs from earlier work [e.g., *Elliott, 1976; Masek and Duncan, 1998*] where the energy dissipation and the work done is also computed at the thrust sheet or mountain belt scale but relying on strongly simplifying assumptions about the geometry of the transitions and the activated deformation mechanisms. Also, as discussed above, the class of transitions to be considered should be extended to include fans, often invoked in the trishear model [*Erslev, 1991*] and more recently as back fans at the lower flat-ramp transition, as proposed independently by *Cristallini and Allmendinger [2002]* and *Buil [2002]*. Thus pressure sensitive flexural slip could provide a mechanical basis for the unification of the usually opposed kink band and trishear kinematic models. It is hoped that these future developments could be the basis of the construction of mechanically balanced cross sections, with the appropriate accounts of rock

rheology, and would complement the now classical kinematic models of folding.

Appendix A: Solution Procedure for Localized Flow Analysis

[51] The objective of this Appendix is to present the weak formulation of the problem and the solution procedure to determine the stress state and the slip rate within the hinge for the two-phase creeping materials described in section 2.

[52] The overall deformation is simple shear and the weak formulation to determine the velocity component $U_1(x_2)$ is

$$\int_0^h \tau(x_2) \frac{\partial \hat{U}_1(x_2)}{\partial x_2} dx_2 = 0, \quad (A1)$$

in which τ and \hat{U}_1 are the unknown shear stress and the virtual velocity, respectively. An approximate solution to equation (A1) is constructed with the finite element method. The stress $\tau(x_2)$ is then seen as a nonlinear function of σ_T , $p(x_2)$, $\dot{\gamma}(x_2)$ and $\omega(x_2)$. This function is known implicitly at any point as the solution of the following set of equations:

$$\begin{aligned} \dot{\gamma} - \frac{1-w^2}{1+w^2} \dot{\gamma}_S - \tau \frac{\dot{\gamma}_{0B}}{\tau_{0B}} \left(\frac{\sigma_e}{\tau_{0B}} \right)^{\frac{1-m_B}{m_B}} &= 0, \\ \dot{\gamma}_S \frac{w}{1+w^2} + (\sigma_T - p) \frac{\dot{\gamma}_{0B}}{2\tau_{0B}} \left(\frac{\sigma_e}{\tau_{0B}} \right)^{\frac{1-m_B}{m_B}} &= 0 \quad (A2) \\ \sigma_e^2 &= \tau^2 + (\sigma_T - p)^2, \end{aligned}$$

where $w(x_2)$ is standing for the velocity along \mathbf{e}_1 normalized by the velocity along \mathbf{e}_2 (i.e., $w(x_2) = U_1(x_2)/V$). The first of these two equations expresses the decomposition of the overall simple shear rate in a slip and a bulk strain rate (equation (15)). The second equation in (A2) states that the overall component D_{11} is zero and thus that the bulk phase has to accommodate creep in the first direction to compensate for the incompatible slip with respect to the overall shear. In these two equations, the equivalent strain rate $\dot{\gamma}_B$ has been replaced by the equivalent stress σ_e , defined as the second invariant of the deviatoric stress, with the power law relation $\sigma_e = \tau_{0B}(\dot{\gamma}_B/\dot{\gamma}_{0B})^{m_B}$, which is generalized to three dimensional creep flow in equation (11).

[53] The solution to the set of equation (A2), complemented by the relation between σ_T and τ in equations (3) and (16), is solved in a three-step procedure. First, it is assumed that slip does not occur and the first equation (A2) provides the pressure $p = \sigma_T$. The equivalent stress σ_e is then determined from the second equation and, with the help of equation (3), the shear stress is determined. The second step consists of checking if the slip criterion defined in equation (13) is satisfied. If yes, the third step is the search by the Newton-Raphson method of the solution to equation (A2) starting from the solution with no slip rate as a first guess. The linearization of equation (A2), required for that solution search, is not presented here for sake of brevity. This linearization is also at the basis of the derivation of the tangent operator $\partial\tau/\partial\dot{\gamma}$ which is required to solve the nonlinear equilibrium equation (A1). The final solution in terms of stress τ is uniform over the hinge once

equilibrium is satisfied and is the stress τ_T defined in equation (16).

[54] **Acknowledgments.** We would like to thank D. Frizon de Lamotte (Université de Cergy-Pontoise, France) for stimulating discussions on folding in mountain belts and J.-P. Gratier (LGIT, Grenoble, France) for his insight in the rheology of sedimentary rocks. Constructive discussions with members of the Geology and Geochemistry Division of IFP, France, on the need to introduce concepts of mechanics in kinematical models are gratefully acknowledged. J.R. Rudnicki (Northwestern University) and F. Salvini (University of Roma III) are thanked for their constructive reviews.

References

- Berger, P., and A. M. Johnson, First order analysis of deformation of a thrust sheet moving over a ramp, *Tectonophysics*, 70, T9–T24, 1980.
- Berger, P., and A. M. Johnson, Folding of passive layers and forms of minor structures near terminations of blind thrust systems—Application to the central Appalachian blind thrust, *J. Struct. Geol.*, 4(3), 343–353, 1982.
- Bodin, L., Bandes de cisaillement en thermo-viscoplasticité dynamique: applications à l'usinage et à la rupture ductile des métaux, Doctoral thesis, Univ. of Metz, Metz, France, 1996.
- Bonini, M., D. Sokoutis, G. Mulugeta, and E. Katrivanos, Modelling hanging wall accommodation above rigid thrust ramps, *J. Struct. Geol.*, 22, 1165–1179, 2000.
- Boyer, S. E., Styles of folding within thrust sheets: Examples from the Appalachian and Rocky mountains of the U.S.A. and Canada, *J. Struct. Geol.*, 8(3/4), 325–339, 1986.
- Buil, D., L'approche cinématique du plissement naturel: Intérêts et limites: Développements autour de la notion de "Trishear", Doctoral thesis, Univ. of Cergy-Pontoise, Cergy-Pontoise, France, 2002.
- Chadwick, P., *Continuum Mechanics: Concise Theory and Problems*, 2nd corr. and enl. ed., Dover, Mineola, N. Y., 1999.
- Chester, J. S., J. M. Logan, and J. H. Spang, Influence of layering and boundary conditions on fault-bend fold and fault propagation folding, *Geol. Soc. Am. Bull.*, 103, 1059–1072, 1991.
- Collomb, P., and M. Donzeau, Relations entre kink-bands décimétriques et fractures de socle dans l'hercynien des monts d'Ougarta (Sahara Occidental, Algérie), *Tectonophysics*, 24, 213–242, 1974.
- Cristallini, E. O., and R. W. Allmendinger, Backlimb trishear: A kinematic model for curved folds developed over angular fault bends, *J. Struct. Geol.*, 24, 289–295, 2002.
- Elliott, D., The energy balance and deformation mechanisms of thrust sheets, *Philos. Trans. R. Soc. London, Ser. A*, 283, 289–312, 1976.
- Erickson, J. P., and W. R. Jamison, Viscous-plastic finite element models of fault-bend folds, *J. Struct. Geol.*, 17(4), 561–573, 1995.
- Erickson, J. P., L. M. Strayer, and J. Suppe, Initiation and reactivation of faults during movement over a thrust-fault ramp: numerical mechanical models, *J. Struct. Geol.*, 23, 11–23, 2001.
- Erslev, E. A., Trishear fault-propagation folding, *Geology*, 9, 617–620, 1991.
- Geiser, P., Mechanisms of thrust propagation: Some examples and implications for the analysis of overthrust terranes, *J. Struct. Geol.*, 10(8), 829–845, 1988.
- Gratier, J.-P., Le fluage des roches par dissolution-cristallisation sous contrainte, dans la croûte supérieure, *Bul. Soc. Géol. Fr.*, 164(2), 267–287, 1993.
- Johnson, K. M., and A. M. Johnson, Mechanical models of trishear-like folds, *J. Struct. Geol.*, 24, 277–287, 2002a.
- Johnson, K. M., and A. M. Johnson, Mechanical analysis of the geometry of forced folds, *J. Struct. Geol.*, 24, 401–410, 2002b.
- Lan, L., and P. Hudleston, The effect of anisotropy on the shape of fault-bend folds, *Proc. Int. Geol. Congr.*, 30th(14), 106–118, 1997.
- Masek, J. G., and C. C. Duncan, Minimum-work mountain building, *J. Geophys. Res.*, 103, 907–917, 1998.
- Medwedeff, D. A., Growth fault-bend folding at southeast Lost Hills, San Joaquin Valley, California, *AAPG Bull.*, 73, 54–67, 1989.
- Merchant, E., Basic mechanics of the metal-cutting process, *J. Appl. Mech.*, 12, 168–175, 1944.
- Merchant, E., Mechanics of the metal cutting process. II. Plasticity conditions in orthogonal cutting, *J. Appl. Phys.*, 16, 318–324, 1945.
- Merle, O., and N. Abidi, Approche expérimentale du fonctionnement des rampes émergentes, *Bul. Soc. Géol. Fr.*, 166(5), 439–450, 1995.
- Molinari, A., and D. Dudzinski, Stationary shear band in high-speed machining, *C. R. Acad. Sci.*, 315, 399–405, 1992.
- Morse, J., Deformation in ramp regions of overthrust faults: Experiments with small-scale rock models, in *29th Annual Field Conference Guidebook*, pp. 457–470, Wyo. Geol. Assoc., Casper, 1977.
- Renard, F., J.-P. Gratier, and B. Jamtveit, Kinetics of crack-sealing, intergranular pressure solution, and compaction around active faults, *J. Struct. Geol.*, 22, 1395–1407, 2000.
- Rich, J. L., Mechanics of low-angle overthrust faulting as illustrated by Cumberland thrust block, Virginia, Kentucky, and Tennessee, *Am. Assoc. Pet. Geol. Bull.*, 18, 1584–1596, 1934.
- Rudnicki, J. W., and J. R. Rice, Conditions for the localization of deformation in pressure-sensitive dilatant materials, *J. Mech. Phys. Solids*, 23, 371–394, 1975.
- Serra, S., Styles of deformation in the ramp regions of overthrust faults, in *29th Annual Field Conference Guidebook*, pp. 487–498, Wyo. Geol. Assoc., Casper, 1977.
- Shaw, J. H., and J. Suppe, Active faulting and growth folding in the Eastern Santa Barbara Channel, California, *Geol. Soc. Am. Bull.*, 106, 607–626, 1994.
- Suppe, J., Geometry and kinematics of fault-bend folding, *Am. J. Sci.*, 283, 684–721, 1983.
- Suppe, J., and D. A. Medwedeff, Fault-propagation folding, *Geol. Soc. Am. Bull. Abstr. Programs*, 16, 670, 1984.
- Suppe, J., and D. A. Medwedeff, Geometry and kinematics of fault-propagation folding, *Ecolgae Geol. Helv.*, 83, 409–454, 1990.
- Wiltshko, D. V., Thrust sheet deformation at a ramp: summary and extensions of an earlier model, in *Thrust and Nappe Tectonics*, edited by K. R. McClay and N. J. Price, *Spec. Publ. Geol. Soc.*, 9, 55–63, 1981.

B. Maillot, Département des Sciences de la Terre, UMR CNRS 7072, Université de Cergy-Pontoise, 8 Avenue du Parc, F-95031 Cergy-Pontoise Cedex, France. (Bertrand.Maillot@geol.u-cergy.fr)

Y. M. Leroy, Laboratoire de Mécanique des Solides, UMR CNRS 7649, École Polytechnique, F-91128 Palaiseau Cedex, France. (leroy@lms.polytechnique.fr)